



UNIVERSITY OF LEEDS

This is a repository copy of *Widespread marine euxinia along the western Yangtze Platform caused by oxygen minimum zone expansion during the Capitanian mass extinction*.

White Rose Research Online URL for this paper:

<https://eprints.whiterose.ac.uk/204182/>

Version: Accepted Version

Article:

Zhang, B., Yao, S., Poulton, S.W. et al. (4 more authors) (2023) Widespread marine euxinia along the western Yangtze Platform caused by oxygen minimum zone expansion during the Capitanian mass extinction. *Global and Planetary Change*, 230. 104273. ISSN 0921-8181

<https://doi.org/10.1016/j.gloplacha.2023.104273>

© 2023, Elsevier. This manuscript version is made available under the CC-BY-NC-ND 4.0 license <http://creativecommons.org/licenses/by-nc-nd/4.0/>.

Reuse

This article is distributed under the terms of the Creative Commons Attribution-NonCommercial-NoDerivs (CC BY-NC-ND) licence. This licence only allows you to download this work and share it with others as long as you credit the authors, but you can't change the article in any way or use it commercially. More information and the full terms of the licence here: <https://creativecommons.org/licenses/>

Takedown

If you consider content in White Rose Research Online to be in breach of UK law, please notify us by emailing eprints@whiterose.ac.uk including the URL of the record and the reason for the withdrawal request.



eprints@whiterose.ac.uk
<https://eprints.whiterose.ac.uk/>

1 **Widespread marine euxinia along the western Yangtze Platform caused by**
2 **oxygen minimum zone expansion during the Capitanian mass extinction**

3 Bolin Zhang^{1,2,3*}, Suping Yao³, Simon W. Poulton⁴, Paul B. Wignall⁴,

4 Tianchen He⁵, Yijun Xiong⁴, Wenxuan Hu³

5 ¹ *State Key Laboratory of Oil and Gas Reservoir Geology and Exploitation & Institute*
6 *of Sedimentary Geology, Chengdu University of Technology, Chengdu 610059, China*

7 ² *Key Laboratory of Deep-time Geography and Environment Reconstruction and*
8 *Applications of Ministry of Natural Resources, Chengdu University of Technology, Chengdu*
9 *610059, China*

10 ³ *Key Laboratory of Surficial Geochemistry, Ministry of Education, School of Earth*
11 *Sciences and Engineering, Nanjing University, Nanjing 210023, China*

12 ⁴ *School of Earth and Environment, University of Leeds, Leeds LS2 9JT, UK*

13 ⁵ *College of Oceanography, Hohai University, Nanjing 210024, China*

14
15 ***corresponding author: zhangbolin@cdut.edu.cn (B. Zhang)**

16
17 **Abstract**

18 The development of widespread marine anoxic and/or euxinic conditions has been
19 proposed as a likely driver of the mid-Capitanian mass extinction. However, the driving
20 mechanisms and spatiotemporal evolution of anoxia/euxinia remain poorly constrained. In
21 order to decipher changes in marine redox conditions and their possible influence on the mid-
22 Capitanian biotic crisis, we applied multiple geochemical indicators to three sections across a

23 shelf-to-basin transect in the Middle Permian Kuhfeng and Lower Yinying formations of the
24 Lower Yangtze Basin, South China. Our integrated Fe speciation and redox-sensitive trace
25 element data suggest that euxinic waters dynamically coexisted at intermediate depths on the
26 western margin of the Yangtze Platform, with oxygenated surface waters and ferruginous
27 deeper waters providing compelling evidence for a redox structure similar to an oxygen
28 minimum zone (OMZ). The synthesis of a five-stage spatiotemporal evolution of redox
29 conditions, coupled with changes in upwelling and hydrographic restriction, indicates
30 particularly intensified euxinia and an expanded OMZ across the shelf-basin transect during
31 the middle Capitanian. Long-lasting anoxia-euxinia was likely maintained by enhanced
32 phosphorus cycling, with sluggish ocean circulation due to collapsed upwelling and enhanced
33 restriction under climate warming intensifying the euxinic conditions. Through a comparison
34 of available global data, we infer that widespread anoxia-euxinia was prevalent in the middle
35 Capitanian due to expanded OMZ conditions. Expanded anoxia and euxinia in shelf and slope
36 environments occurred concurrently with an ongoing biotic crisis suggesting that these redox
37 changes were a contributory factor.

38

39 **Keywords:** Middle Permian; South China; Redox conditions; Fe speciation

40

41 **1. Introduction**

42 The mid-Capitanian (or end-Guadalupian) biotic crisis, is one of the most severe biotic
43 events of the Phanerozoic (comparable to the “Big Five” Phanerozoic mass extinctions; e.g.,
44 Stanley, 2016), although its timing, nature and causes are all debated. Proposed causal
45 mechanisms include regression (e.g., Jin et al., 1994; Chen et al., 2009), global cooling (e.g.,
46 Isozaki et al. 2007), marine anoxia (e.g., Zhang et al., 2015; Wei et al., 2016, 2019; Smith et
47 al., 2020), or the effects of the Emeishan Large Igneous Province eruptions (ELIP, e.g., Kaiho
48 et al., 2005, 2023; Sun et al., 2010; Wignall et al., 2009; Huang et al., 2019). However, while
49 no consensus has been reached, the development of marine anoxia has frequently been invoked
50 as consequential (e.g., Saitoh et al., 2014; Bond et al., 2015; Wei et al., 2016, 2019; Fujisaki et
51 al., 2019; Smith et al., 2020; Song et al., 2023).

52 During the Capitanian, marine anoxia was apparently widespread, but with distinct
53 temporal and regional variability (e.g., Zhang et al., 2019a; Fujisaki et al., 2019; Song et al.,
54 2023). Previous studies have shown that anoxic-euxinic conditions were present prior to the
55 late Capitanian at intermediate ocean depths around the margin of the South China continent
56 (Saitoh et al. 2014; Wei et al., 2019; Zhang et al., 2019a, b, 2021). Expansion of this mid-depth
57 water oxygen minimum zone (OMZ) saw the spread of oxygen-poor conditions into shallow
58 waters prior to and/or during the extinction (Saitoh et al. 2014; Bond et al. 2015; Zhang et al.
59 2015; Wei et al., 2016, 2019). However, better constraints on the spatial distribution of anoxia-
60 euxinia in the water column and its dynamic evolution through this period are required to
61 understand its potential role as a kill mechanism during the mid-Capitanian crisis.

62 The driving mechanisms responsible for the development of intensified anoxic and/or

63 euxinic conditions during the mid-Capitanian extinction are not fully understood. Divergent
64 opinions propose either the expansion of OMZ-type conditions caused by increased upwelling
65 and productivity (e.g., Saitoh et al., 2014; Zhang et al., 2019a), or decreased upwelling but
66 increased terrigenous nutrient input during global warming (e.g., Chen et al., 2011; Zhang et
67 al., 2021). Alternatively, basinal anoxia may have expanded during marine regression (e.g.,
68 Wei et al., 2019; Smith et al., 2020). Modern oceanic-climate models suggest that OMZ
69 expansion can result in the shoaling of sulfidic waters (e.g., Stramma et al., 2008), while
70 upwelling-driven OMZ expansion and oceanic anoxia have been linked to other mass
71 extinctions (e.g., Late Ordovician-Early Silurian, Zou et al., 2018). However, much less is
72 known about the redox state and spatiotemporal evolution of Middle Permian upwelling-driven
73 OMZ settings and controlling mechanisms.

74 Here, we aim to decipher spatiotemporal changes of marine redox conditions in the eastern
75 Paleo-Tethys Ocean (South China) during the Middle Permian, and to evaluate the role of such
76 changes in the mid-Capitanian crisis. We apply a multi-proxy approach based on iron speciation
77 and redox-sensitive trace elements (particularly Mo and U) to analyze redox changes in three
78 sections that accumulated along a shelf-to-basin transect in the Lower Yangtze upwelling
79 region. A Middle Permian OMZ-type redox structure and its dynamic evolution are
80 reconstructed.

81

82 **2. Geological setting**

83 **2.1 Paleogeography and studied sections**

84 During the Middle Permian, the Lower Yangtze Basin was located on the northwestern

85 margin of the Yangtze Platform (South China) and was open to the Paleo-Tethys Ocean that
86 lay to the northwest (Fig. 1a, Wang and Jin, 2000). A widespread upwelling system has been
87 proposed to have developed along this margin throughout the Middle Permian (Kametaka et al.
88 2005; Yao et al. 2015; Shi et al., 2016; Zhang et al., 2021, 2023). This is confirmed by the
89 lithological character of the strata, which are typical of those found beneath upwelling zones
90 (e.g., phosphate nodules and rhythmic chert-mudstone couplets), the paleontological
91 assemblage (radiolarians and sponge spicules), geochemical evidence (i.e., $Cd/Mo > 0.1$ and
92 $Co \times Mn < 0.4$), and the paleoenvironmental conditions (i.e., high surface primary productivity
93 and middle water-depth anoxic conditions) as indicated by the studies on the Kuhfeng
94 Formation (Lv and Zhai, 1990; Winguth et al., 2002; Kametaka et al., 2005; Lv et al., 2010;
95 Yao et al., 2015; Shi et al., 2016; Zhang et al., 2018, 2021, 2022a, 2023). In addition, the
96 Permian paleogeographic and paleoclimatic modeling predicted that over 70% of the areas
97 along the northwestern margin of the Yangtze Platform were favorable locations for upwelling
98 (Golonka et al., 1994).

99 A northwest-southeast transect through the Lower Yangtze basin captures a full range of
100 settings from continental shelf, through slope to deep basin (Fig. 1b). Two well-exposed
101 sections (Pingdingshan and Qinglongshan) and a newly-drilled core (Gangdi) (Fig. 2) provide
102 a shelf-to-basin transect (Figs. 1b-c). The Pingdingshan (PDS) section was mainly deposited
103 in an open-marine, lower slope–basin setting (Fig. 2) (Kametaka et al., 2005, 2009), whereas
104 the Qinglongshan (QLS) section records sedimentary succession in relatively shallower water
105 outer shelf facies (Fig. 2), although it was below fair-weather wave base and far from shore,
106 on a broad continental shelf (Figs. 1d-e; Zhang et al., 2020). The Gangdi (GD) core

107 accumulated on an open outer shelf setting with a good connection to the Paleo-Tethys Ocean
108 during the early-middle Guadalupian (Figs. 1d and 2), but the location is inferred to have
109 become silled later, during the Capitanian, due to tectonic intrashelf subsidence (Fig. 1e; Zhang
110 et al., 2022b). An explanation of the above sedimentary environments can be found in Fig. 2
111 and Supplementary Tables S1-S3 and Fig. S1. In addition, previous studies have also confirmed
112 that, based on typical minerals (e.g., glauconite pellets and phosphate nodules) and radiolarian
113 faunas (He et al., 1999; Kametaka et al., 2005, 2009), the water depth range in the Lower
114 Yangtze region during the deposition of the Kuhfeng Formation was approximately 50-500 m,
115 which is comparable to the water depth (~100–900 m) at which the OMZ develops in the
116 modern ocean (e.g., Scholz, 2018).

117

118 **2.2 Age constraints and stratigraphic correlation**

119 The Lower Yangtze Basin provides a relatively continuous Middle Permian stratigraphic
120 record, with both deep (Kuhfeng Formation) and shallow (Yinping Formation) marine units.
121 The Kuhfeng Formation consists of cyclically interbedded chert and mudstone, which are
122 attributed to orbital forcing (Yao et al., 2015), whereas the Yinping Formation records shallow,
123 coastal clastic deposition composed mainly of black to pale-grey mudstone, shale and siltstone
124 (Zhang et al., 2020, 2021). The Kuhfeng Formation is subdivided into three lithologically-
125 distinct members: the Lower Phosphate Nodule-bearing Mudstone Member (LPMM), the
126 Middle Chert-Mudstone Member (MCMM), and the Upper Mudstone Member (UMM). The
127 Lower Yinping Formation is divided into two members: the Lower Shale Member (LSM) and
128 the Middle Shale Member (MSM) (Fig. 2). Intrabasinal correlation has been achieved using a

129 well-established lith-, bio- and chemostratigraphic framework (Fig. 2; Zhang et al., 2020).

130 Conodonts (e.g., *Jinogondolella nankingensis*) and ammonoids (e.g., *Nodogastrioceras*
131 *discum*, *Erinoceras sp*) discovered in the basal beds of the Kuhfeng Formation suggest an early
132 Middle Permian age (e.g., Kametaka et al., 2009; Wu et al., 2017). Three radiolarian
133 assemblage zones established in the Kuhfeng Formation also indicate a Roadian-Capitanian
134 age (Fig. 2; Kametaka et al., 2009; Zhang et al., 2020). Furthermore, high-precision zircon U-
135 Pb ages of 272.95 ± 0.11 Ma (Wu et al., 2017) and 261.08 ± 0.14 Ma (Wu, 2020) from tuff
136 beds at the base and top of the Kuhfeng Formation, respectively, also suggest that the Kuhfeng
137 Formation is of Middle Permian age and accumulated over 11 Myrs (Fig. 2). Finally, a high-
138 resolution $\delta^{13}\text{C}_{\text{org}}$ chemostratigraphic framework through these studied sections (Zhang et al.,
139 2020) can be correlated globally (Fig. 2). The negative excursions in $\delta^{13}\text{C}_{\text{org}}$ from the LPMM
140 to the middle MCMM suggest a Roadian interval (e.g., Shen et al., 2020), which was followed
141 by a Wordian–early Capitanian positive excursion in the upper MCMM and lower UMM (Fig.
142 2; Zhang et al., 2020). A subsequent negative $\delta^{13}\text{C}_{\text{org}}$ excursion, best seen in the upper UMM
143 to the LSM of the GD core data (Fig. 2). This may coincide with the major negative shift in
144 $\delta^{13}\text{C}_{\text{carb}}$ values of many worldwide sections (e.g., Wignall et al., 2009; Bond et al., 2010; Zhang
145 et al., 2020), indicating the middle Capitanian interval. This inference is supported by boundary
146 tuff U-Pb ages of 261.08 ± 0.14 Ma (Fig. 2; Wu, 2020), which is consistent with our previous
147 LA-ICP-MS dating results (261.6 ± 1.6 Ma) on the same sample (PDS-5; Zhang et al., 2019b).
148 Following this negative excursion, a rapid positive $\delta^{13}\text{C}_{\text{org}}$ shift in the MSM suggests the late
149 Capitanian interval (Fig. 2).

150

151 **3. Samples and methods**

152 A total of 230 samples were collected at approximately 0.7–1.0 m intervals from the
153 freshest exposures of the PDS section, GD core and QLS section. All samples were crushed
154 and ground into powders for subsequent geochemical analyses. Total Al concentrations were
155 determined by an ARL9900 X-ray fluorescence spectrometry (XRF), with analytical
156 uncertainty < 1%, and trace elements were determined after bulk rock total dissolution on a
157 Finnigan Element 2 inductively coupled plasma mass spectrometer (ICP-MS) with analytical
158 precision better than 5%. Both Al concentration and trace elements were analysed at the State
159 Key Laboratory for Mineral Deposits Research, Nanjing University. Detailed analytical
160 methods for trace and major element analyses are in Supplementary Materials and [Zhang et al.](#)
161 [\(2018\)](#).

162 Highly reactive iron (Fe_{HR}) was determined following the sequential extraction procedure
163 of [Poulton and Canfield \(2005\)](#). The scheme determines operationally-defined Fe pools, and
164 targets Fe in pyrite (Fe_{py}), ferric (oxyhydr)oxides (Fe_{ox}), magnetite (Fe_{mag}) and carbonate
165 phases (Fe_{carb}). Concentrations of Fe_{carb} , Fe_{ox} and Fe_{mag} in sequential extracts were determined
166 via atomic absorption spectrometry (AAS) at University of Leeds, with a relative standard
167 deviation (RSD) of < 5% for all phases. Fe_{py} was extracted using the chromium reduction
168 method ([Canfield et al., 1986](#)) and calculated stoichiometrically based on the pyrite sulfur
169 concentration (S_{py}) assuming a 1:2 Fe:S molar ratio in pyrite. For elemental analyses of total
170 iron (Fe_T), we used a multi-acid digestion (HNO_3 -HF- $HClO_4$) on ashed samples (8 h at 550 °C)
171 before quantification via AAS, with a RSD of < 5% ([Alcott et al., 2020](#)).

172

173 **4. Proxy interpretation**

174 Fe speciation and redox-sensitive trace elements (RSTEs, e.g., Mo and U) are widely used
175 to diagnose local water column redox conditions during sediment deposition (e.g., Tribovillard
176 et al., 2006; Poulton and Canfield, 2011; Scott and Lyons, 2012; Poulton, 2021). The combined
177 use of these redox proxies can provide a robust evaluation of a range of local water-column
178 redox conditions (e.g., Poulton and Canfield, 2011; Poulton, 2021).

179 Generally, Fe_{HR}/Fe_T ratios exceeding 0.38 imply anoxic water column conditions, whereas
180 ratios below 0.22 indicate oxic conditions in the water column (Poulton and Canfield, 2011;
181 Poulton, 2021). For anoxic samples, Fe_{Py}/Fe_{HR} ratios can distinguish euxinic conditions (> 0.8)
182 and possibly euxinic conditions (0.6–0.8) from anoxic, ferruginous conditions (< 0.6) (Poulton,
183 2021). In addition, Fe_T/Al ratios can potentially provide information for evaluating water
184 column redox conditions, since the ratio is commonly considered to remain unaffected by
185 diagenesis (e.g., Lyons and Severmann, 2006). Fe_T/Al ratios above the average oxic
186 Phanerozoic shale value (0.55 ± 0.11) may indicate anoxic water column conditions during
187 deposition, when applied alongside other independent water column redox proxies (Clarkson
188 et al., 2014; Poulton, 2021). However, it is increasingly apparent that Fe_T/Al ratios may be
189 much more variable than previously thought, with a variety of studies identifying particularly
190 low background ratios in sediments delivered to the marine realm, which may subsequently
191 mask enrichments indicative of water column anoxia (e.g., Poulton et al., 2010; Alcott et al.,
192 2022; Li et al., 2022). In addition, there is the potential for intense sedimentary Fe cycling [e.g.,
193 release of Fe^{2+} to the water column and subsequent re-precipitation of a proportion of this Fe^{2+}
194 as Fe (oxyhydr)oxides] under anoxic ferruginous conditions, resulting in elevated Fe_{HR}/Fe_T

195 ratios combined with low Fe_T/Al (e.g., [Li et al., 2022](#)). Thus, while elevated Fe_T/Al ratios
196 provide support for anoxic depositional conditions, lower values should be interpreted with a
197 high degree of caution, particularly when the data contrast with other, more sensitive redox
198 proxies (e.g., Fe speciation, trace metals, biomarkers).

199 In terms of redox-sensitive trace element proxies, we focus here on Mo and U.
200 Molybdenum is particularly useful since it responds to the availability of dissolved sulfide.
201 Under ferruginous conditions, precipitation of Fe minerals such as Fe (oxyhydr)oxides or green
202 rust (e.g., [Zegeye et al., 2012](#)) may draw down Mo through a particulate shuttle mechanism
203 (e.g., [Algeo and Tribovillard, 2009](#); [Tribovillard et al., 2012](#)). However, with sufficient sulfide
204 availability under euxinic conditions, the molybdate anion is converted to particle-reactive
205 thiomolybdate ([Helz et al., 1996](#)). This commonly results in particularly large Mo enrichments
206 in the sediment ([Emerson and Husted, 1991](#); [Helz et al., 1996](#); [Erickson and Helz, 2000](#)).
207 Indeed, the degree of Mo enrichment can help to distinguish permanently euxinic, Mo-replete
208 settings (> 100 ppm), intermittently/seasonally euxinic settings or permanently Mo-depleted
209 euxinic settings (25–100 ppm), and non-euxinic settings (< 25 ppm) ([Tribovillard et al., 2006](#);
210 [Scott and Lyons, 2012](#)). Like Mo, U behaves conservatively under oxic water column
211 conditions, but unlike Mo, U reduction primarily occurs in anoxic sediments, without the
212 requirement for free sulfide, and U may therefore be enriched beneath anoxic bottom waters,
213 regardless of whether euxinic or ferruginous conditions dominate (e.g., [Klinkhammer and](#)
214 [Palmer, 1991](#); [Partin et al., 2013](#)). In addition, Mn–Fe redox cycling near the oxic-anoxic
215 interface can accelerate RSTE enrichments in sediments ([Algeo and Tribovillard, 2009](#)).

216 An upwelling setting can be diagnosed by the combined use of Cd/Mo ratios (> 0.1) and

217 Co×Mn values (< 0.4) (Sweere et al., 2016), with upwelling strength indicated by Cd-Mo
218 relationships (i.e., using a Cd-Mo crossplot; Sweere et al., 2016; Zhang et al., 2021). Empirical
219 data show that sediments from modern perennial or sustained upwelling settings (e.g., the Peru
220 margin) have higher Cd/Mo ratios than those from seasonal or transient upwelling settings (e.g.,
221 the Gulf of California) (Sweere et al., 2016; Zhang et al., 2021). Thus, Cd/Mo ratios of > 0.6 ,
222 $0.1-0.6$, and < 0.1 indicate perennial upwelling, seasonal upwelling, and restricted settings,
223 respectively (Sweere et al., 2016).

224

225 **5. Results and discussion**

226 **5.1 Spatiotemporal variations in redox conditions across the shelf-basin transect**

227 **5.1.1 PDS section**

228 In this lower slope section, ratios of Fe_{HR}/Fe_T range from 0.41 to 1.00 (Figs. 3a and 4a),
229 suggesting dominantly anoxic bottom-water conditions (Poulton and Canfield, 2011), which is
230 supported by dominantly high U concentrations and U_{EF} values (Fig. 3a) (Tribovillard and
231 Algeo, 2012; He et al., 2022). Parts of the section also have elevated Fe_T/Al ratios (> 0.66),
232 providing support for anoxic depositional conditions. However, while some Fe_T/Al ratios fall
233 in the typical zone for oxic deposition (0.55 ± 0.11), many samples have highly depleted ratios,
234 which is a common feature throughout the basinal transect (Fig. 3). This clearly highlights the
235 limitations of using Fe_T/Al as a paleoredox proxy. Low Fe_T/Al samples have elevated Fe_{HR}/Fe_T
236 ratios and elevated U_{EF} values, and generally have low Fe_{py}/Fe_{HR} ratios and low Mo_{EF} values,
237 suggesting anoxic-ferruginous depositional conditions. These specific geochemical
238 characteristics are emerging as a common feature of ferruginous conditions (e.g., Poulton et al.,

239 [2010; Alcott et al., 2022; Li et al., 2022](#)), and imply intense Fe cycling between the water
240 column and shallow sediments (see above; [Li et al., 2022](#)). By contrast, elevated Fe_T/Al ratios
241 commonly coincide with high Fe_{py}/Fe_{HR} ratios and/or high Mo_{EF} values ([Fig. 3](#)), implying at
242 least a degree of euxinia, which would trap diagenetically mobilized Fe^{2+} in the sediment as
243 sulfide phases, thus maintaining primary elevated Fe_T/Al ratios arising from water column
244 precipitation of Fe minerals under anoxic conditions ([Poulton and Canfield, 2011; Raiswell et](#)
245 [al., 2018; Poulton, 2021](#)).

246 On top of these general geochemical redox characteristics, distinct temporal variability is
247 evident in the evolving redox conditions through the lower slope section ([Figs. 3a and 4a-b](#)).
248 In the LPMM, samples with elevated Fe_{py}/Fe_{HR} ratios coincide with relatively low Mo
249 enrichments ([Fig. 4b](#)). While these combined characteristics may indicate a possible degree of
250 euxinia (i.e., weak or intermittent), particularly because Fe_T/Al ratios are also elevated (see
251 above) in the upper LPMM ([Fig. 3a](#)), the low Mo contents could be caused by limited Mo
252 resupply under relatively weak upwelling conditions (see Section 5.2). For the MCMM,
253 dominantly anoxic-ferruginous conditions are indicated throughout most of the interval, with
254 the possible development of intermittent or weak euxinia towards the top ([Figs. 3a and 4a](#)).
255 There is also a zone of elevated Fe_{py}/Fe_{HR} towards the top of the Roadian stage in the MCMM,
256 which coincides with commonly elevated Mo_{EF} values ([Fig. 3a](#)). However, these data fall in
257 the particulate shuttle zone on a Mo_{EF} vs U_{EF} crossplot ([Fig. 5a](#)), suggesting elevated drawdown
258 of Mo due to uptake by Fe (oxyhydr)oxides under ferruginous conditions ([Tribovillard and](#)
259 [Algeo, 2012](#)).

260 In the UMM, there is a peak in Fe_{py}/Fe_{HR} ratios, but this peak falls below the threshold for

261 identification of persistent euxinia (Fig. 3a). Combined with moderate enrichments in Mo, this
262 suggests intermittent euxinia, which progressed to an interval of stronger and more persistent
263 euxinia in the middle of the LSM (Figs. 3a and 4a-b). Enrichments in Fe_{HR}/Fe_T in the MSM,
264 combined with generally low Fe_{py}/Fe_{HR} ratios (Figs. 3a and 4a), and low U_{EF} with moderate
265 Mo_{EF} values (Figs. 3a and 5a), indicates a return to ferruginous conditions, with the progression
266 to lower Fe_{HR}/Fe_T through this interval possibly implying a gradual return to a better ventilated
267 water column in this part of the basin.

268

269 5.1.2 GD core

270 Elevated Fe_{HR}/Fe_T ratios, U concentrations and U_{EF} values persist throughout almost the
271 entirety of the GD core (Fig. 3b), suggesting persistent anoxia (Poulton and Canfield, 2011;
272 Tribovillard and Algeo, 2012; Poulton, 2021). Fe_{py}/Fe_{HR} ratios are high throughout the GD
273 core, implying dominantly euxinic conditions (Figs. 3b and 4c), which in most of the section
274 is supported by elevated Mo_{EF} values (Fig. 3b). However, Mo_{EF} values and Mo concentrations
275 fluctuate considerably, with some samples from the LPMM and MSM possibly indicating
276 ferruginous (or intermittently ferruginous) conditions, based on relationships between Mo
277 concentrations and Fe_{py}/Fe_{HR} ratios (Fig. 4d), as well as Mo_{EF} and U_{EF} values (Fig. 5a).
278 Considerable fluctuations in Mo concentrations through the MCMM, UMM and MSM (Fig.
279 3b), may indicate that the water column fluctuated between highly and weakly/intermittently
280 euxinic (Scott and Lyons, 2012). However, despite the prevalence of euxinia, Fe_T/Al ratios are
281 often below the normal range for oxic marine sediments (Fig. 3b), although ratios generally do
282 not reach the very lowest levels found under ferruginous conditions in the deeper, slope setting

283 (Fig. 3a). Since euxinia is more effective at trapping Fe^{2+} in the sediments, relative to the
284 possibility for remobilization back to the water column under ferruginous conditions (Poulton
285 and Canfield, 2011; Poulton, 2021), the prevalence of low Fe_T/Al suggests that the background
286 ratios in detrital sediments delivered to this region were low. Thus, Fe_T/Al ratios across the
287 basin appear to have been affected both by recycling of Fe^{2+} back to the water column in some
288 ferruginous intervals (see above), as well as low detrital values, which reinforces the difficulties
289 inherent in using Fe_T/Al as a reliable paleoredox proxy.

290 The relatively low Mo concentrations observed in some euxinic sections may provide
291 further insight into paleoenvironmental conditions, since Mo drawdown can also be affected
292 by hydrographic restriction (e.g., McArthur et al., 2008). Generally, the degree of basin
293 restriction is related to eustatic changes, which could have caused significant restriction owing
294 to reduced water depths over sills at the basin margin (Zhang et al., 2020, 2022a, b). A higher
295 degree of restriction during this interval is potentially indicated by low Mo/TOC ratios (Fig.
296 5b; see Section 5.2), which are similar to those observed in euxinic sediments of restricted
297 basins (e.g., Algeo and Lyons, 2006). Limited resupply of Mo via deep water renewal would
298 have resulted in a reduced local Mo seawater budget, resulting in less uptake of Mo per unit of
299 organic matter compared to fully connected ocean basins (Algeo and Lyons, 2006; McArthur
300 et al., 2008). Thus, persistent euxinia could have gradually drawn down the Mo concentration
301 of seawater, resulting in relatively low Mo concentrations in the euxinic sediments, which is
302 also supported by the relationship between $\text{Fe}_{py}/\text{Fe}_{HR}$ and Mo (Fig. 4d).

303

304 **5.1.3 QLS section**

305 High Fe_{HR}/Fe_T ratios (> 0.38) and U_{EF} values occur throughout the QLS section (Fig. 3c),
306 suggesting persistent bottom water anoxia across the outer shelf during the Middle Permian.
307 However, low Fe_{py}/Fe_{HR} ratios coupled with low Mo concentrations and Mo_{EF} values, indicate
308 anoxic-ferruginous conditions during deposition of the LPMM and MCMM (Fig. 3c). Through
309 the UMM, sporadic enrichments in Fe_{py}/Fe_{HR} , Mo concentrations and Mo_{EF} values indicate
310 fluctuations between anoxic ferruginous, weak/intermittent euxinia, and more strongly euxinic
311 conditions, which is consistent with strong fluctuations in Fe_T/Al ratios as discussed above
312 (Figs. 3c and 4e-f). Water column redox conditions continued to fluctuate through the LSM
313 and MSM, with high peaks in Mo coupled with Fe_{py}/Fe_{HR} ratios that fall to below 0.6 after
314 initial high values (Figs. 3c and 4e-f), likely indicating dominantly ferruginous conditions with
315 short-term intervals of euxinia, which is supported by data plotting in the particulate shuttle
316 zone on the U_{EF} vs Mo_{EF} crossplot (Fig. 5a).

317

318 **5.1.4 Synthesis of the spatiotemporal redox records**

319 The data through our three studied sites document both short-term and longer-term spatio-
320 temporal changes across the Lower Yangtze shelf-basin transect (Fig. 6). The Roadian-
321 Wordian interval (i.e., LPMM–lower UMM) is characterized by laterally variable redox
322 conditions, with euxinia dominating in mid-water depths (shelf margin), and anoxic-
323 ferruginous conditions being more dominant in both deeper (lower slope) and shallower (outer
324 shelf) waters. The early-middle Capitanian stage (i.e., upper UMM–LSM) is marked by more
325 widespread, particularly enhanced euxinia across the shelf-basin transect (Fig. 6). Following

326 the middle Capitanian (i.e., MSM), redox conditions returned to a dominantly anoxic-
327 ferruginous state.

328

329 **5.2 Hydrographic response to variability in Guadalupian upwelling**

330 Widespread upwelling has been proposed along the Eastern Paleo-Tethys Margin during
331 the Middle Permian (Yao et al. 2015; Shi et al., 2016; Zhang et al., 2018, 2021, 2022a). Our
332 previous studies on both the PDS section and GD core (Fig. 7a-b), combined with new data
333 from the QLS section (Fig. 7c; and see the Supplementary Materials for further discussion),
334 indicate relatively strong upwelling (sometimes seasonal) in the LPMM, MCMM and lower
335 UMM (i.e., Roadian-Wordian), but with a gradual transition from a seasonal upwelling setting
336 to a more restricted environment through the UMM and across the boundary with the LSM (i.e.,
337 early-middle Capitanian) (Zhang et al., 2021, 2022a). This may indicate a significant
338 weakening or collapse in the upwelling system (Zhang et al., 2021, 2022a). Following a sea
339 level lowstand, upwelling increased in the upper LSM and MSM (i.e., late Capitanian; Fig. 7).
340 This evolution of the Guadalupian upwelling system along the western Yangtze Platform is
341 supported by Cd vs Mo and Al vs (Co×Mn) crossplots (Fig. 8).

342 The $M_{\text{OEF}}-U_{\text{EF}}$ covariation patterns can be used to help evaluate the degree of
343 hydrographic restriction (e.g., Algeo and Tribovillard, 2009). As shown in Fig. 5a, almost all
344 LPMM samples plot in the unrestricted marine zone. Similarly, most samples of the MCMM
345 and lower UMM have predominantly high M_{OEF} and U_{EF} values, which mainly scatter around
346 the unrestricted marine trend, but with a few values trending towards the particulate shuttle
347 field (Fig. 5a). This reflects an open marine upwelling system with a weak or intermittently

348 operating shuttle during this time interval. For the upper UMM and LSM, most samples show
349 high Mo_{EF} values relative to U enrichments, defining a covariation pattern that falls between
350 the unrestricted marine trend and the particulate shuttle field (Fig. 5a). This enhanced
351 particulate shuttle is consistent with strong but temporally variable water-mass exchange across
352 this gradually restricted basin. Further up-section, most samples of the MSM cluster close to
353 the area of unrestricted conditions, with low Mo/U ratios ($< SW$), except for samples of the
354 QLS section that are still dominated by a particulate shuttle influence (Fig. 5a).

355 Although Mo/TOC ratios in sediments can also provide insight into the degree of water-
356 mass restriction (Algeo and Lyons, 2006; Algeo and Rowe, 2012), this approach is not suitable
357 for continental margin upwelling settings, in which low Mo/TOC ratios (e.g., $\sim 6 \pm 3$ of modern
358 Namibian shelf, Algeo and Lyons, 2006) are a consequence of redox rather than hydrographic
359 controls (e.g., Algeo and Rowe, 2012). Thus, low Mo/TOC ratios (average 1.66, 3.81 and 8.08
360 for the PDS section, GD core and QLS section, respectively) observed in the Kuhfeng
361 Formation (Figs 5b and 7) can be attributed to insufficient H_2S build-up due to rapid water
362 mass exchange under the strong upwelling system at this time (e.g., Algeo and Lyons, 2006).
363 By contrast, with the weakening of upwelling, slightly increased Mo/TOC ratios (average 21.96,
364 10.89 and 35.70 for the PDS section, GD core and QLS section, respectively) during the
365 transition to the Yinping Formation (Figs 5b and 7) likely relate to the abrupt changes in redox
366 conditions (e.g., Algeo and Rowe, 2012), which were a potential response to enhanced
367 restriction.

368 Taken together, accompanying the changes in upwelling, the observed patterns in our three
369 studied sites show spatially and temporally variable water-mass exchange across the Lower

370 Yangtze basin. The Roadian-Wordian stage is characterized by laterally unconfined circulation
371 and strong watermass exchange in both deeper and shallower waters, whereas the early-middle
372 Capitanian stage is marked by weakened deeper-water ventilation and enhanced shallow-water
373 restriction, with an effective particulate shuttle.

374

375 **5.3 Reconstruction and dynamic evolution of an upwelling-driven OMZ-type redox** 376 **structure**

377 Detailed examination of paleoredox data for our three studied sections provides
378 compelling evidence for strong temporal and spatial variability in marine redox conditions
379 along the Middle Permian Yangtze Platform margin (Figs. 3 and 6). A clear euxinic state is also
380 evident in the Hexian area (Zhang et al., 2019a), located between Nanjing and Chaohu, and the
381 Xiaolao area (Wei et al., 2019), situated between the Gangdi and Chaohu (Figs. 1c-d and 6).
382 Thus, a synthesis of these laterally varying redox conditions points to an upwelling-driven
383 OMZ-type oceanic structure, in which anoxic-ferruginous to euxinic redox conditions
384 dynamically coexisted at intermediate depths (Figs. 6a-e).

385 The location and dimensions of this “OMZ-type redox structure” appears to have
386 fluctuated: five phases of redox evolution on the eastern margin of the Paleo-Tethys Ocean can
387 be determined (Fig. 6). As the main period of Late Paleozoic Ice Age (LPIA) weakened, the
388 Middle Permian saw the transition to a greenhouse climate (e.g., Chen et al., 2013; Zhang et
389 al., 2021), leading to a wide range of upwelling systems around the world (Beauchamp and
390 Baud, 2002). With rapid transgression during the early Roadian, vigorous upwelling occurred
391 on the Eastern Paleo-Tethys margin (Kametaka et al., 2005; Yao et al., 2015; Zhang et al., 2018,

392 2021, 2022a), triggering an OMZ (Fig. 6a). This process may have been exacerbated by
393 increased nutrient input driven by enhanced chemical weathering under gradual climate
394 warming (e.g., Zhang et al., 2021). Thus, a fluctuating “euxinic wedge” developed at mid-
395 depths on the north-west shelf margin of South China from this interval.

396 Until the end of the Wordian stage, anoxic-ferruginous water column conditions were a
397 prevalent feature throughout deposition in both shallow-water shelf and deep-water slope
398 settings, whereas euxinia only occurred at intermediate depths, dominantly on shelf margins
399 (Figs. 6a-b). Strong watermass exchange with unconfined circulation dominated across the
400 basin with the enhanced development of this open marine upwelling system during this interval.
401 Subsequently, marine regression gradually occurred from the early Capitanian stage, as
402 inferred from increased terrestrial inputs, which may have resulted in a weaker connection to
403 the open ocean (Zhang et al., 2020, 2022b). During the early-middle Capitanian, all five
404 sections show parallel evidence for enhanced euxinia, which was coupled to the weakened
405 upwelling and enhanced hydrographic restriction, suggesting an expansion of the OMZ (Fig.
406 6c). This zone prevailed until the middle Capitanian (i.e., *Jinogondolella xuanhanensis*
407 conodont zone), and the intensified euxinia encroached to a maximum lateral extent to within
408 ~250 km from the paleoshoreline (Fig. 6d). Subsequently, the area of euxinia contracted
409 probably driven by regression (Zhang et al., 2022b), resulting in a less extensive OMZ typified
410 by dominantly ferruginous conditions (Fig. 6e).

411

412 **5.4 Potential drivers of long-lasting OMZ anoxia and the spread of euxinia**

413 Generally, the dynamics of nutrient cycling and the degree of oxygen depletion are closely
414 linked (e.g., [Algeo and Ingall, 2007](#); [Schobben et al., 2020](#)). As a key limiting nutrient for
415 marine productivity, phosphorus (P) is a potential driver for eutrophication-induced oxygen
416 depletion and thus the development of widespread anoxia (e.g., [Meyer et al., 2008](#); [Schobben
417 et al., 2020](#)). Here, we consider TOC/TP and P/Al ratios to provide insight into the potential
418 significance of P cycling across the Middle Permian Lower Yangtze Basin (e.g., [Algeo and
419 Ingall, 2007](#)), recognizing that the presence of detrital P exerts an added complication to these
420 records (e.g., [Guilbaud et al., 2020](#); [Schobben et al., 2020](#); [Qiu et al., 2020](#)).

421 Extremely low TOC/TP ratios (well below the Redfield ratio of 106:1) combined with
422 relatively high P/Al values in the LPMM ([Fig. 7](#)), suggest low recycling of P (e.g., [Guilbaud et
423 al., 2020](#); [Schobben et al., 2020](#)). This is consistent with drawdown of P under the dominantly
424 ferruginous conditions envisaged for this interval ([Fig. 7](#)), which resulted in the extensive
425 formation of phosphate nodules (e.g., [Kametaka et al., 2009](#); [Zhang et al., 2020](#)). Indeed, the
426 formation of phosphate nodules at this time, coupled with high P/Al, suggests a high
427 bioavailable P flux to the basin (either through enhanced chemical weathering or intense
428 upwelling), which may have initiated the development of anoxic conditions (e.g., [Schobben et
429 al., 2020](#); [Qiu et al., 2022](#)).

430 During deposition of the MCMM, TOC/TP ratios increase dramatically, to values greatly
431 in excess of the Redfield ratio, while the P/Al ratios decrease to values below, or approaching,
432 average shale ([Fig. 7](#)). This suggests very efficient recycling of P back to the water column
433 during preferential release of P from organic matter during microbial remineralization, coupled

434 with release of P during the reductive dissolution of Fe (oxyhydr)oxides (e.g., [Ingall et al., 1993](#);
435 [Ingall and Jahnke, 1997](#); [Slomp et al., 2002](#); [Algeo and Ingall, 2007](#)). Both these processes are
436 stimulated by the production of dissolved sulfide, which is consistent with the enhanced
437 development of euxinia at this time ([Fig. 6](#)). Enhanced P recycling, combined with strong
438 watermass mixing under the influence of the perennial upwelling, likely resulted in the rapid
439 transport of bioavailable P into shallower productive waters, further fueling increased
440 productivity and thus the organic flux to the sediments (e.g., [Algeo and Ingall, 2007](#)). Overall,
441 efficient recycling of P would have resulted in a positive feedback loop where intensified
442 euxinia was sustained, thereby promoting further P cycling and elevated productivity.

443 During the UMM, TOC/TP ratios generally decrease, particularly in the more proximal
444 settings (i.e., GD core and QLS section), but values still considerably exceed the Redfield ratio
445 ([Fig. 7](#)). This decrease may not be related to lithological change, because no correlation was
446 observed between TOC/TP ratios and Al contents (not shown) suggesting there was no
447 influence of detrital input variations. Large fluctuations of TOC/TP ratios within the same
448 lithological member excludes the possible effect of lithological changes. P/Al ratios also
449 decline over this interval, and these combined observations suggest efficient P recycling back
450 to the water column as euxinic conditions continued to expand ([Fig. 6](#)). In addition, enhanced
451 weathering driven by climate warming, as indicated by increased values of chemical index of
452 alteration (i.e., CIA; [Zhang et al., 2021, 2022a](#)), likely also promoted an increased influx of P
453 to the coastal area at this time, further enhancing productivity and oxygen consumption in
454 proximal settings ([Zhang et al., 2021](#)). This is supported by additional evidence for particularly
455 high rates of productivity at this time from trace element systematics ([Zhang et al., 2021](#)).

456 Sluggish basinal circulation, coupled with rapid climate warming and a gradual collapse in
457 upwelling during this interval, may have further accelerated the spread of euxinic conditions.

458 Across the LSM, TOC/TP ratios decline, particularly in the deeper water sections, while
459 P/Al ratios show a transient increase (Fig. 7). This implies more efficient trapping of reactive
460 P as authigenic phases (e.g., fluorapatite) during diagenesis, which is supported by the strong
461 positive correlations between Ca and P contents in both the PDS and QLS sections ($R^2 = 0.91$
462 and 0.79, respectively; Fig. S2). Changes in the P cycling described above may have been
463 driven by the particularly enhanced development of euxinia at this time (Fig. 6). Expanded
464 euxinia commonly lowers water column sulfate concentrations, which has the effect of
465 enabling more phosphate to be trapped in the sediment as authigenic phases (e.g., Xiong et al.,
466 2019). It is noteworthy that the drawdown of recycled P mainly occurred in the proximal (i.e.,
467 QLS section) and distal settings (i.e., PDS section) (Fig. 7), indicating a strong redox-controlled
468 nutrient shuttle (e.g., Schobben et al., 2020), operating from the heart of the euxinic zone in the
469 GD core, across the shelf-basin transect (Fig. 6). As sea level dropped to its lowstand during
470 MSM deposition, the OMZ declined in extent and conditions were dominantly ferruginous,
471 restricting P recycling and productivity. This effectively constrained the maximum spatial
472 extent and intensity of anoxia.

473 **5.5 Impact of widespread anoxia-euxinia on the mid-Capitanian biotic crisis**

474 **5.5.1 Global redox links to OMZ expansion in the Lower Yangtze basin**

475 The widespread anoxic conditions across the Lower Yangtze basin during the early-middle
476 Capitanian support an expansion and intensification of an OMZ, which ultimately increased
477 the frequency of sulfidic water incursions onto the shelf. This OMZ expansion also likely

478 occurred in the Middle (e.g., Tianfengping and Maocaojie sections; [Shi et al., 2016](#); [Wei et al.,](#)
479 [2016](#)) and Upper (e.g., Chaotian section, [Saitoh et al., 2014](#)) Yangtze area during the early-
480 middle Capitanian ([Fig. 9](#)), indicating extensive anoxic/euxinic conditions developed along the
481 eastern Paleo-Tethys ocean margin. Elsewhere, the southeast Yangtze Platform margin (e.g.,
482 the Penglaitan section), which faced the western edge of Panthalassa, also shows evidence for
483 long-term dysoxic to anoxic conditions in the early-middle Capitanian (from the *J. altudaensis*
484 to *J. xuanhanensis* conodont zones; [Wei et al., 2016](#); [Song et al., 2023](#)), with the development
485 of euxinia at the end of Capitanian ([Fig. 9](#); [Zhang et al., 2015](#); [Wei et al., 2016](#); [Song et al.,](#)
486 [2023](#)). Also, the northern and western margins of Pangea (e.g., Opal Creek and Boreal Realm
487 sections), which were located in the western upwelling zone of the Panthalassic ocean,
488 exhibited an intensification of oxygen depletion, or even euxinic conditions, in the middle to
489 late Capitanian ([Fig. 9](#); e.g., [Schoepfer et al., 2013](#); [Zhang et al., 2015](#); [Bond et al., 2015, 2020](#);
490 [Smith et al., 2020](#)). Unlike these continental shelf margin settings, the abyssal mid-Panthalassa
491 (e.g., Gujo-Hachiman section) was dominated by oxic conditions ([Fujisaki et al., 2019](#)), but
492 also appears to have experienced suboxic conditions in the late Capitanian ([Fig. 9](#); [Onoue et](#)
493 [al., 2021](#)). Therefore, taking into account the widespread development of strong upwelling
494 related to vigorous global-ocean circulation during the Middle Permian (e.g., [Beauchamp and](#)
495 [Baud, 2002](#)), these records indicate that intensified anoxic to euxinic conditions mainly
496 occurred in continental shelf margin settings, and were hence related to OMZ expansion during
497 the middle Capitanian. Accompanied by global regression, the OMZ would have allowed
498 encroachment of sulfidic waters onto the continental shelves until the end of the Capitanian.

499

500 **5.5.2 Effect of anoxia-euxinia on the mid-Capitanian biotic crisis**

501 From the Roadian to Wordian stages, the dynamic euxinic water mass that developed along
502 the shelf margin likely placed a major constraint on communities living in deeper-water and
503 ocean-facing habitats, and thus likely accounts for the loss or turnover of radiolarians (e.g.,
504 *Pseudoalbaillella*) and sponge spicules (e.g., Zhang et al., 2019b). During the early-middle
505 Capitanian, intensified mid-depth euxinic waters coupled with the OMZ expansion, resulted in
506 the spread of anoxia into previously oxygenated areas of the shelf, progressively restricting
507 habitable shallower shelf habitats (e.g., Clapham et al., 2009). This incursion during the middle
508 Capitanian would have created widespread inhospitable conditions for benthic shelf
509 communities leading to the observed gradual decrease in marine invertebrate diversity (e.g.,
510 rugose corals; Fig. 9) (e.g., Clapham et al., 2009; Shen and Shi, 2009; Song et al., 2023). Rapid
511 sea level drop accompanied by the eruption of ELIP could compress their habitat range along
512 the continental margins (e.g., Wei et al., 2016), further stressing benthic communities (Fig. 9),
513 despite some areas (e.g., the Laibin area) also showed the recovery of benthic faunas during
514 this interval (e.g., Kaiho et al., 2005; Chen et al., 2009; Huang et al., 2019). In combination
515 with these ecological stresses, the development of widespread anoxia-euxinia around the world
516 during the end-Capitanian likely led to significant selective taxonomic loss of genera,
517 eventually driving some benthic and even nektonic fauna to extinction (Fig. 9).

518

519 **6. Conclusions**

520 In order to unravel the redox history of eastern Paleo-Tethys Ocean (South China) during
521 the Middle Permian, and to decipher possible influences on the mid-Capitanian biotic crisis,

522 we evaluated Fe speciation, redox-sensitive trace metals systematics, and P cycling for three
523 different water-depth sections/cores across a shelf-to-basin transect in the Lower Yangtze
524 region. Our results provide compelling evidence for strong temporal and spatial variability in
525 marine redox conditions along the Yangtze Platform margin. A synthesis of these varying
526 marine redox conditions points to an OMZ-type setting, in which euxinic waters dynamically
527 coexisted at intermediate depths, with commonly ferruginous deeper waters. We construct a
528 five-phase spatiotemporal evolution of redox conditions. Vigorous upwelling in the Roadian-
529 Wordian lead to the development of an OMZ on the continental margin dominated by anoxic-
530 ferruginous conditions in unrestricted setting. The intensity of upwelling declined in the
531 Capitanian and yet the OMZ expanded, with euxinia becoming more important. Enhanced
532 phosphorus cycling across the basin could be a potential driver of the Guadalupian long-lasting
533 OMZ anoxia and subsequent spread of euxinia during the Capitanian. During the Capitanian,
534 ocean circulation and upwelling declined enhancing restriction which, together with increased
535 terrestrial nutrient supply, caused intensification of euxinic conditions in marginal shelf seas.
536 The spread and shallowing of the euxinic waters coincided with the mid-Capitanian biotic crisis,
537 suggesting these redox changes were a key driving mechanism.

538

539 **Acknowledgements**

540 We thank Dr. Gang Shi for providing samples and Dr. Biao Liu for assistance in the
541 fieldwork. Prof. Shuzhong Shen and Dr. Zhong Han is especially acknowledged for their
542 helpful and constructive suggestions. Funding was provided by the National Natural Science
543 Foundation of China (Grant Nos. 42202130, 41888101 and 42072152). We acknowledge Prof.

544 Yadong Sun and one anonymous reviewer for their comments that substantially improved this
545 work, as well as Prof. Maoyan Zhu for editorial handling.

546

547 **References**

548 Alcott, L.J., Krause, A.J., Hammarlund, E.U., Bjerrum, C.J., Scholz, F., Xiong, Y., Hobson, A.J., Neve, L.,

549 Mills, B.J.W., März, C., Schnetger, B., Bekker, A., Poulton, S. W., 2020. Development of iron speciation

550 reference materials for palaeoredox analysis. *Geostand. Geoanal. Res.* 44, 581–591.

551 Alcott, L.J., Mills, B.J.W., Bekker, A., Poulton, S. W., 2022. Earth’s Great Oxidation Event facilitated by the

552 rise of sedimentary phosphorus recycling. *Nat. Geosci.* 15, 210–216.

553 Algeo, T.J., Ingall, E., 2007. Sedimentary C_{org}: P ratios, paleocean ventilation, and Phanerozoic atmospheric

554 pO₂. *Palaeogeogr. Palaeoclimatol. Palaeoecol.* 256, 130–155.

555 Algeo, T.J., Lyons, T., 2006. Mo-total organic carbon covariation in modern anoxic marine environments:

556 Implications for analysis of paleoredox and paleohydrographic conditions. *Paleoceanography* 21,

557 PA1016.

558 Algeo, T.J., Rowe, H., 2012. Paleoceanographic applications of trace-metal concentration data. *Chem. Geol.*

559 324, 6–18.

560 Algeo, T.J., Tribovillard, N., 2009. Environmental analysis of paleoceanographic systems based on

561 molybdenum-uranium covariation. *Chem. Geol.* 268, 211–225.

562 Beauchamp, B., Baud, A., 2002. Growth and demise of Permian biogenic chert along northwest Pangea:

563 evidence for end-Permian collapse of thermohaline circulation. *Palaeogeogr. Palaeoclimatol.*

564 *Palaeoecol.* 184, 37–63.

565 Bond, D.P.G., Hilton, J., Wignall, P.B., Ali, J.R., Stevens, L.G., Sun, Y., Lai, X., 2010. The Middle Permian

566 (Capitanian) mass extinction on land and in the oceans. *Earth Sci. Rev.* 102, 100–116.

567 Bond, D.P.G., Wignall, P.B., Joachimski, M.M., Sun, Y., Savov, I., Grasby, S.E., Beauchamp, B., Blomeier,
568 D.P.G., 2015. An abrupt extinction in the Middle Permian (Capitanian) of the Boreal Realm
569 (Spitsbergen) and its link to anoxia and acidification. *Geol. Soc. Am. Bull.* 127, 1411–1421.

570 Bond, D.P.G., Wignall, P.B., Grasby, S.E., 2020. The Capitanian (Guadalupian, Middle Permian) mass
571 extinction in NW Pangea (Borup Fiord, Arctic Canada): A global crisis driven by volcanism and anoxia.
572 *Geol. Soc. Am. Bull.* 132, 931–942.

573 Canfield, D.E., Raiswell, R., Westrich, J.T., Reaves, C.M., Berner, R.A., 1986. The use of chromium
574 reduction in the analysis of reduced inorganic sulfur in sediments and shales. *Chem. Geol.* 54, 149–155.

575 Chen, B., Joachimski, M.M., Sun, Y.D., Shen, S.Z., Lai, X.L., 2011. Carbon and conodont apatite oxygen
576 isotope records of Guadalupian-Lopingian boundary sections: climatic or sea-level signal? *Palaeogeogr.*
577 *Palaeoclimatol. Palaeoecol.* 311, 145–153.

578 Chen, B., Joachimski, M.M., Shen, S.Z., Lambert, L.L., Lai, X.L., Wang, X.D., Chen, J., Yuan, D.X., 2013.
579 Permian ice volume and palaeoclimate history: oxygen isotope proxies revisited. *Gondwana Res.* 24,
580 77–89.

581 Chen, Z.Q., George, A.D., Yang, W.R., 2009. Effects of middle-late Permian sea-level changes and mass
582 extinction on the formation of the Tieqiao skeletal mound in the Laibin area, South China. *Aust. J. Earth*
583 *Sci.* 56, 745–763.

584 Clapham, M.E., Shen, S.Z., Bottjer, D.J., 2009. The double mass extinction revisited: reassessing the severity,
585 selectivity, and causes of the end-Guadalupian biotic crisis (Late Permian). *Paleobiology* 35, 32–50.

586 Clarkson, M.O., Poulton, S.W., Guilbaud, R., Wood, R.A., 2014. Assessing the utility of Fe/Al and Fe-
587 speciation to record water column redox conditions in carbonate-rich sediments. *Chem. Geol.* 382, 111–

588 122.

589 Emerson, S.R., Huested, S.S., 1991. Ocean anoxia and the concentrations of molybdenum and vanadium in
590 seawater. *Mar. Chem.* 34 (3-4), 177–196.

591 Erickson, B.E., Helz, G.R., 2000. Molybdenum (VI) speciation in sulfidic waters: Stability and lability of
592 thiomolybdates. *Geochim. Cosmochim. Acta* 64 (7), 1149–1158

593 Fujisaki, W., Sawaki, Y., Matsui, Y., Yamamoto, S., Isozaki, Y., Maruyama, S., 2019. Redox condition and
594 nitrogen cycle in the Permian deep mid-ocean: A possible contrast between Panthalassa and Tethys.
595 *Glob. Planet. Chang.* 172, 179–199.

596 Golonka, J., Ross, M.I., Scotese, C.R., 1994. Phanerozoic paleogeographic and paleoclimatic modeling maps.
597 In: Embry, A.F., Beauchamp, B., Glass, D.J. (Eds.), *Pangea: Global Environments and Resources*.
598 Canadian Society of Petroleum Geology Memoir, 17, pp. 1–47.

599 Guilbaud, R., Poulton, S.W., Thompson, J., Husband, K.F., Zhu, M., Zhou, Y., Shields, G. A., Lenton, T.M.,
600 2020. Phosphorus-limited conditions in the early Neoproterozoic ocean maintained low levels of
601 atmospheric oxygen. *Nat. Geosci.* 13, 236–301.

602 He, T., Wignall, P.B., Newton, R.J., Atkinson, J.W., Keeling, J.F.J., Xiong, Y., Poulton, S.W., 2022. Extensive
603 marine anoxia in the European epicontinental sea during the end-Triassic mass extinction. *Glob. Planet.*
604 *Chang.* 210, 103771.

605 He, W., Wu, S., Zhang, K., Pu, J., 1999. Classification of radiolarian fossil zones and environmental analysis
606 of Gufeng Formation in Lower Yangtze region. *Jiangsu Geol* 23, 17–23 (in Chinese with English
607 abstract).

608 Helz, G.R., Miller, C.V., Charnock, J.M., Mosselmans, J.F.W., Patrick, R.A.D., Garner, C. D., Vaughan, D.J.,
609 1996. Mechanism of molybdenum removal from the sea and its concentration in black shales: EXAFS

610 evidence. *Geochim. Cosmochim. Acta* 60, 3631–3642.

611 Huang, Y.G., Chen, Z.Q., Wignall, P.B., Grasby, S., Zhao, L.S., Wang, X.D., Kaiho, K., 2019. Biotic
612 responses to volatile volcanism and environmental stresses over the Guadalupian-Lopingian (Permian)
613 transition. *Geology* 47, 175–178.

614 Ingall E., Jahnke R., 1997. Influence of water-column anoxia on the elemental fractionation of carbon and
615 phosphorus during sediment diagenesis. *Mar. Geol.* 139, 219–229.

616 Ingall E. D., Bustin R. M., Van Cappellen P., 1993. Influence of water column anoxia on the burial and
617 preservation of carbon and phosphorus in marine shales. *Geochim. Cosmochim. Acta* 57, 303–316.

618 Isozaki, Y., Kawahata, H., Ota, A., 2007. A unique carbon isotope record across the Guadalupian-Lopingian
619 (Middle-Upper Permian) boundary in mid-oceanic paleo-atoll carbonates: the high-productivity
620 “Kamura event” and its collapse in Panthalassa. *Glob. Planet. Chang.* 55, 21–38.

621 Jin, Y., Zhang, J., Shang, Q., 1994. Two phases of the end-Permian mass extinction. *Can. Soc. Petrol. Geol.*
622 17, 813–822.

623 Kaiho, K., Chen, Z.Q., Ohashi, T., Arinobu, T., Sawada, K., Cramer, B.S., 2005. A negative carbon isotope
624 anomaly associated with the earliest Lopingian (Late Permian) mass extinction. *Palaeogeogr.*
625 *Palaeoclimatol. Palaeoecol.* 223, 172–180.

626 Kaiho, K., Grasby, S.E., Chen, Z.-Q., 2023. High-temperature combustion event spanning the
627 Guadalupian–Lopingian boundary terminated by soil erosion. *Palaeogeogr. Palaeoclimatol. Palaeoecol.*
628 618, 1–11.

629 Kametaka, M., Nagai, H., Zhu, S., Takebe, M., 2009. Middle Permian radiolarians from Anmenkou, Chaohu,
630 Northeastern Yangtze platform, China. *Island Arc* 18, 108–125.

631 Kametaka, M., Takebe, M., Nagai, H., Zhu, S., Takayanagi, Y., 2005. Sedimentary environments of the

632 Middle Permian phosphorite-chert complex from the northeastern Yangtze platform, China; the
633 Kuhfeng Formation: a continental shelf radiolarian chert. *Sediment. Geol.* 174, 197–222.

634 Klinkhammer, G., Palmer, M.R., 1991. Uranium in the oceans: where it goes and why. *Geochim. Cosmochim.*
635 *Acta* 55, 1799–1806.

636 Li, S., Wignall, P.B., Poulton, S.W., Hedhli, M., Grasby, S.E., 2022. Carbonate shutdown, phosphogenesis
637 and the variable style of marine anoxia in the late Famennian (Late Devonian) in western Laurentia.
638 *Palaeogeogr. Palaeoclimatol. Palaeoecol.* 589, 110835.

639 Lv, B.Q., Zhai, J.Z., 1990. Sedimentation of anoxic environments under transgression and upwelling process
640 in Early Permian in Lower Yangtze area. *China Sci. Bull.* 35, 1193–1198.

641 Lv, B.Q., Cai, J.G., Liu, F., Shao, L., Wang, H.G., Quan, Q.S., 2010. Upwelling deposits at the marginal
642 slope of a carbonate platform in Qixia stage and its relation with hydrocarbon source rocks. *Marine*
643 *Geol. Quat. Geol.* 30, 109–118 (in Chinese with English abstract).

644 Lyons, T.W., Severmann, S., 2006. A critical look at iron paleoredox proxies: new insights from modern
645 euxinic marine basins. *Geochim. Cosmochim. Acta* 70, 5698–722.

646 McArthur, J.M., Algeo, T.J., Van de Schootbrugge, B., Li, Q., Howarth, R.J., 2008. Basinal restriction, black
647 shales, Re-Os dating, and the Early Toarcian (Jurassic) oceanic anoxic event. *Paleoceanography* 23,
648 PA4217.

649 Meyer, K.M., Kump, L.R., Ridgwell, A., 2008. Biogeochemical controls on photic-zone euxinia during the
650 end-Permian mass extinction. *Geology* 36, 747–750.

651 Onoue, T., Soda, K., Isozaki, Y., 2021. Development of deep-sea anoxia in Panthalassa during the Lopingian
652 (Late Permian): insights from redox-sensitive elements and multivariate analysis. *Front. Earth Sci.* 8,
653 613126.

654 Partin, C.A., Bekker, A., Planavsky, N.J., Scott, C.T., Gill, B.C., Li, C., Podkovyrov, V., Maslov, A.,
655 Konhauser, K.O., Lalonde, S.V., Love, G.D., Poulton, S.W., Lyons, T.W., 2013. Large-scale fluctuations
656 in Precambrian atmospheric and oceanic oxygen levels from the record of U in shales. *Earth Planet. Sci.*
657 *Lett.* 369-370, 284–293.

658 Poulton, S.W., Canfield, D.E., 2005. Development of a sequential extraction procedure for iron: implications
659 for iron partitioning in continentally derived particulates. *Chem. Geol.* 214, 209–221

660 Poulton, S.W., Canfield, D.E., 2011. Ferruginous conditions: a dominant feature of the ocean through earth's
661 history. *Elements* 7, 107–112.

662 Poulton, S.W., Fralick, P.W., Canfield, D.E., 2010. Spatial variability in oceanic redox structure 1.8 billion
663 years ago. *Nat. Geosci.* 3, 486–490.

664 Poulton, S.W., 2021. *The Iron Speciation Paleoredox Proxy*. Cambridge Univ. Press pp. 1–20.

665 Qiu, Z., Zou, C., Mills, B.J.W., Xiong, Y., Tao, H., Lu, B., Liu, H., Xiao, W., Poulton, S.W., 2022. A nutrient
666 control on expanded anoxia and global cooling during the Late Ordovician mass extinction. *Commun.*
667 *Earth Environment*, 3, 82.

668 Raiswell, R., Hardisty, D.S., Lyons, T.W., Canfield, D.E., Owens, J.D., Planavsky, N.J., Poulton, S.W.,
669 Reinhard, C.T., 2018. The iron paleoredox proxies: A guide to the pitfalls, problems and proper practice.
670 *Am. J. Sci.* 318, 491–526.

671 Saitoh, M., Ueno, Y., Isozaki, Y., Nishizawa, M., Shozugawa, K., Kawamura, T., Yao, J.X., Ji, Z.S., Takai,
672 K., Yoshida, N., Matsuo, M., 2014. Isotopic evidence for water-column denitrification and sulfate
673 reduction at the end-Guadalupian (Middle Permian). *Glob. Planet. Chang.* 123, 110–120.

674 Schobben, M., Foster, W.J., Sleveland, A.R.N., Zuchuat, V., Svensen, H.H., Planke, S., Bond, D.P.G.,
675 Marcelis, F., Newton, R.J., Wignall, P.B., Poulton, S.W., 2020. A nutrient control on marine anoxia

676 during the end-Permian mass extinction. *Nat. Geosci.* 13, 640–646.

677 Schoepfer, S.D., Henderson, C.M., Garrison, G.H., Foriel, J., Ward, P.D., Selby, D., Hower, J.C., Algeo, T.J.,
678 Shen, Y., 2013. Termination of a continent-margin upwelling system at the Permian-Triassic boundary
679 (Opal Creek, Alberta, Canada). *Glob. Planet. Chang.* 105, 21–35.

680 Scholz, F., 2018. Identifying oxygen minimum zone-type biogeochemical cycling in Earth history using
681 inorganic geochemical proxies. *Earth Sci. Rev.* 184, 29–45.

682 Scott, C., Lyons, T.W., 2012. Contrasting molybdenum cycling and isotopic properties in euxinic versus non-
683 euxinic sediments and sedimentary rocks: refining the paleoproxies. *Chem. Geol.* 324–325, 19–27.

684 Shen, S.Z., Shi, G.R., 2009. Latest Guadalupian brachiopods from the Guadalupian/Lopingian boundary
685 GSSP section at Penglaitan in Laibin, Guangxi, South China and implications for the timing of the pre-
686 Lopingian crisis. *Palaeoworld* 18, 152–161.

687 Shen, S.Z., Yuan, D.X., Henderson, C.M., Wu, Q., Zhang, Y.C., Zhang, H., Mu, L., Ramezani, J., Wang,
688 X.D., Lambert, L.L., Erwin, D.H., Hearst, J.M., Xiang, L., Chen, B., Fan, J.X., Wang, Y., Wang, W.Q.,
689 Qi, Y.P., Chen, J., Qie, W.K., Wang, T.T., 2020. Progress, problems and prospects: an overview of the
690 guadalupian series of South China and North America. *Earth Sci. Rev.* 211, 103412.

691 Shi, L., Feng, Q.L., Shen, J., Ito, T., Chen, Z.Q., 2016. Proliferation of shallow-water radiolarians coinciding
692 with enhanced oceanic productivity in reducing conditions during the Middle Permian, South China:
693 evidence from the Kuhfeng Formation of western Hubei Province. *Palaeogeogr. Palaeoclimatol.*
694 *Palaeoecol.* 444, 1–14.

695 Slomp, C.P., Thompson, J., de Lange, G.J., 2002. Enhanced regeneration of phosphorus during formation of
696 the most recent eastern Mediterranean sapropel (S1). *Geochim. Cosmochim. Acta* 66, 1171–1184.

697 Smith, P.B., Larson, T., Martindale, C.T., Kerans, C., 2020. Impacts of basin restriction on geochemistry and

698 extinction patterns: A case from the Guadalupian Delaware Basin, USA. *Earth Planet. Sci. Lett.* 530,
699 115876.

700 Song, H.Y., Algeo, T.J., Song, H.J., Tong, J.N., Wignall, P.B., Bond, D.P.G., Zheng, W., Chen, X.M.,
701 Romaniello, S.J., Wei, H.Y., Anbar, A.D., 2023. Global oceanic anoxia linked with the Capitanian
702 (Middle Permian) marine mass extinction. *Earth Planet. Sci. Lett.* 610, 118128.

703 Stanley, S.M. 2016. Estimates of the magnitudes of major marine mass extinctions in earth history. *Proc.*
704 *Natl. Acad. Sci. U.S.A.* 113, E6325–E6334.

705 Stramma, L., Johnson, G. C., Sprintall, J., Mohrholz, V., 2008. Expanding oxygen-minimum zones in the
706 tropical oceans. *Science* 320, 655–658.

707 Sun, Y., Lai, X., Wignall, P.B., Widdowson, M., Ali, J.R., Jiang, H., Wang, W., Yan, C., Bond, D.P.G., Vedrine,
708 S., 2010. Dating the onset and nature of the Middle Permian Emeishan large igneous province eruptions
709 in SW China using conodont biostratigraphy and its bearing on mantle plume uplift models. *Lithos* 119,
710 20–33.

711 Sweere, T., van den Boorn, S., Dickson, A.J., Reichart, G.J., 2016. Definition of new trace-metal proxies for
712 the controls on organic matter enrichment in marine sediments based on Mn, Co, Mo and Cd
713 concentrations. *Chem. Geol.* 441, 235–245.

714 Tribouillard, N., Algeo, T.J., Lyons, T., Riboulleau, A., 2006. Trace metals as paleoredox and
715 paleoproductivity proxies: An update. *Chem. Geol.* 232, 12–32.

716 Tribouillard, N., Algeo, T.J., Baudin, F., Riboulleau, A., 2012. Analysis of marine environmental conditions
717 based on molybdenum-uranium covariation - applications to Mesozoic paleoceanography. *Chem. Geol.*
718 324–325, 46–58.

719 Wang, J., Jin, Y.G., 2000. Permian palaeogeographic evolution of the Jiangnan Basin, South China.

720 Palaeogeogr. Palaeoclimatol. Palaeoecol. 160, 35–44.

721 Wei, H.Y., Wei, X.M., Qiu, Z., Song, H.Y., Shi, G., 2016. Redox conditions across the G-L boundary in
722 South China: evidence from pyrite morphology and sulfur isotopic compositions. *Chem. Geol.* 440, 1–
723 14.

724 Wei, H.Y., Tang, Z.W., Yan, D.T., Wang, J.G., Roberts, A.P., 2019. Guadalupian (Middle Permian) ocean
725 redox evolution in South China and its implications for mass extinction. *Chem. Geol.* 530, 119318.

726 Wignall, P.B., 2015. *The worst of times: how life on Earth survived eighty million years of extinctions.*
727 Princeton University Press.

728 Wignall, P.B., Sun, Y.D., Bond, D.P.G., Izon, G., Newton, R.J., Veldrine, S., Widdowson, M., Ali, J.R., Lai,
729 X.L., Jiang, H.S., Cope, H., Bottrell, S.H., 2009. Volcanism, mass extinction, and carbon isotope
730 fluctuations in the Middle Permian of China. *Science* 324, 1179–1182.

731 Winguth, A.M.E., Heinze, C., Kutzbach, J.E., Maier-Reimer, E., Mikolajewicz, U., Rowley, D., Rees, A.,
732 Ziegler, A.M., 2002. Simulated warm polar currents during the middle Permian. *Paleoceanography* 17,
733 9-1–9-18.

734 Wu, Q., Ramezani, J., Zhang, H., Wang, T.T., Yuan, D.X., Mu, L., Zhang, Y.C., Li, X.H., Shen, S.Z., 2017.
735 Calibrating the Guadalupian Series (Middle Permian) of South China. *Palaeogeogr. Palaeoclimatol.*
736 *Palaeoecol.* 466, 361–372.

737 Wu, Q., 2020. High-precision zircon U-Pb geochronological studies of the Permian ash beds from China and
738 North America (Ph.D. Thesis). Univ. of Sci. and Technol. of China pp. 25–46 (in Chinese with English
739 abstract).

740 Xiong, Y. J., Guilbaud, R., Peacock, C. L., Cox, R. P., Canfield, D. E., Krom, M. D., Poulton, S. W., 2019.
741 Phosphorus cycling in Lake Cadagno, Switzerland: A low sulfate euxinic ocean analogue. *Geochim.*

742 Cosmochim. Acta 251, 116–135.

743 Yao, X., Zhou, Y.Q., Hinnov, L.A., 2015. Astronomical forcing of a Middle Permian chert sequence in
744 Chaohu, South China. *Earth Planet. Sci. Lett.* 422, 206–221.

745 Zegeye A., Bonneville S., Benning L. G., Sturm A., Fowle D. A., Jones C. A., Canfield D. E., Ruby C.,
746 MacLean L. C., Nomosatryo S., Crowe S. A. and Poulton S. W., 2012. Green rust formation controls
747 nutrient availability in a ferruginous water column. *Geology* 40, 599–602.

748 Zhang, B., Yao, S., Wignall, P., Hu, W., Ding, H., Liu, B., Ren, Y., 2018. Widespread coastal upwelling along
749 the Eastern Paleo-Tethys Margin (South China) during the Middle Permian (Guadalupian): Implications
750 for organic matter accumulation. *Mar. Pet. Geol.* 97, 113–126.

751 Zhang, B., Yao, S., Hu, W., Ding, H., Liu, B., Ren, Y., 2019a. Development of a high-productivity and
752 anoxic-euxinic condition during the late Guadalupian in the Lower Yangtze region: Implications for the
753 mid-Capitanian extinction event. *Palaeogeogr. Palaeoclimatol. Palaeoecol.* 531, 108630.

754 Zhang, B., Yao, S., Wignall, P. B., Hu, W., Liu, B., Ren, Y., 2019b. New timing and geochemical constraints
755 on the Capitanian (Middle Permian) extinction and environmental changes in deep-water settings:
756 Evidence from the Lower Yangtze region of South China. *J. Geol. Soc.* 176, 588–608.

757 Zhang, B., Yao, S., Mills, B.J.W., Wignall, P. B., Hu, W., Liu, B., Ren, Y., Li, L., 2020. Middle Permian
758 organic carbon isotope stratigraphy and the origin of the Kamura Event. *Gondwana Res.* 79, 217–232.

759 Zhang, B., Wignall, P. B., Yao, S., Hu, W., Liu, B., 2021. Collapsed upwelling and intensified euxinia in
760 response to climate warming during the Capitanian (Middle Permian) mass extinction. *Gondwana Res.*
761 89, 31–46.

762 Zhang B., Yao, S., Hu, W., Han, Z., Liao, Z., Liu, B., Lan, M., 2022a. Middle Permian palaeoclimatic-
763 palaeoceanographic evolution and its controls on organic matter accumulation in the Lower Yangtze

764 upwelling region. *Int. J. Coal Geol.* 264, 104132.

765 Zhang, B., Yao, S., Ma, A., Hu, W., Liu, B., Yang, W., 2022b. New geochemical constraints on the
766 development of active continental margin in Southeast China during the Middle Permian and its tectonic
767 implications. *Gondwana Res.* 103, 458–472.

768 Zhang, B., Cao, J., Mu, L., Yao, S., Hu, W., Huang, H., Lang, X., Liao, Z., 2023. The Permian Chert Event
769 in South China: New geochemical constraints and global implications. *Earth Sci. Rev.* 244, 104513.

770 Zhang, G.J., Zhang, X.L., Li, D.D., Farquhar, J., Shen, S.Z., Chen, X.Y., Shen, Y.A., 2015. Widespread
771 shoaling of sulfidic waters linked to the end-Guadalupian (Permian) mass extinction. *Geology* 43,
772 1091–1094.

773 Zou, C.N., Qiu, Z., Poulton, S.W., Dong, D.Z., Wang, H.Y., Chen, D.Z., Lu, B., Shi, Z.S., Tao, H.F., 2018.
774 Ocean euxinia and climate change “double whammy” drove the Late Ordovician mass extinction.
775 *Geology* 46, 535–538.

776 **FIGURE CAPTIONS**

777 **Fig. 1.** (a) Late Guadalupian global paleogeography. Base map from Ron Blakey
778 (<http://cpgeosystems.com>). (b) Late Guadalupian paleogeographic reconstruction of South
779 China (modified from Yao et al., 2015 and Zhang et al., 2022b). (c) Late Guadalupian
780 paleogeographic reconstruction of the Lower Yangtze area showing section/core localities (red
781 stars). (d–e) Schematic basin cross-section for the Roadian-Wordian and Capitanian Lower
782 Yangtze area, showing the sedimentary facies and relative position of studied sections. Yellow
783 dots and stars indicate sections with redox records from the literature. Abbreviations: PDS =
784 Pingdingshan section, GD = Gangdi core, QLS = Qinglongshan section, HX = Hexian core,
785 XL = Xiaolao, TFP = Tianfengping, MCJ = Maocaojie, CT = Chaotian, TQ = Tieqiao, PLT =
786 Penglaitan, BF = Borup Fiord, BR = Boreal Realm, OC = Opal Creak, DW = Delaware, WT =
787 West Texas, FWB = fair-weather wave base.

788

789 **Fig.2.** Middle Permian lithology and $\delta^{13}\text{C}_{\text{org}}$ chemostratigraphic stratigraphy of the Kuhfeng
790 and Lower Yinping Formation in the Lower Yangtze region (modified from Zhang et al., 2020).
791 The geological timescale is based on Yao et al. (2015), Wu et al. (2017), Zhang et al. (2020),
792 Shen et al. (2020), and Wu (2020). The change in relative water depth is modified from Zhang
793 et al. (2022b). The CA-ID-TIMS U-Pb age of PDS-5 is from Wu (2020). Abbreviations:
794 LPMM = Lower Phosphate Nodule-bearing Mudstone Member, MCMM = Middle Chert-
795 Mudstone Member, UMM = Upper Mudstone Member, LSM = Lower Shale Member, MSM
796 = Middle Shale Member, USM = Upper Shale Member, LSSM = Lower Siltstone-Sandstone
797 Member, S.E. = sedimentary environment, SP = shallow-water ramp, OS = outer shelf, US =

798 upper slope, MS = middle slope, LS = lower slope, BS= basin, CS = coastal setting.

799

800 **Fig. 3.** Redox proxy data for the PDS section (a), GD core (b), and QLS section (c). Green
801 dashed lines indicate the boundary between the Kuhfeng and Yinping formations, and red
802 dashed lines indicate diagnostic thresholds for different redox conditions (after Lyons and
803 Severmann, 2006; Poulton and Canfield, 2011; Scott and Lyons, 2012; Poulton, 2021).
804 Abbreviations: Fm. = Formation.

805

806 **Fig. 4.** Crossplots of Fe_{py}/Fe_{HR} vs Fe_{HR}/Fe_T , and Mo vs Fe_{py}/Fe_{HR} for the PDS section (a–b),
807 GD core (c–d) and QLS section (e–f). Abbreviations: Fm. = Formation.

808

809 **Fig. 5.** Crossplots of Mo_{EF} vs U_{EF} (a), and Mo vs TOC (b) for the three studied sections. The
810 average Mo/U weight ratio of seawater is 3.1 (the Mo/U molar ratio is 7.5–7.9; Algeo and
811 Tribovillard, 2009). Abbreviations: Fm. = Formation.

812

813 **Fig. 6.** Conceptual model for the spatiotemporal evolution of redox conditions along the studied
814 shelf-to-basin transect. The redox records of HX and XL are from Zhang et al. (2019a) and
815 Wei et al. (2019), respectively. Abbreviations: Ser. = Series, Stg. = Stage, Fm. = Formation,
816 *Sw. han.* = *Sweetognathus Hanzhongensis*, *P. longl.* – *P. fus.* = *Pseudoalbaillella longtanensis* –
817 *Pseudoalbaillella fusiformis*, *F. schol.* – *R. uralicus* = *Follicucullus scholasticus* –
818 *Ruzhencevispongus uralicus*, *J. posts.* – *J. altuda.* = *Jinogondolella postserrat* – *Jinogondolella*
819 *altudaensis*, *J. prexua.* – *J. xuan.* = *Jinogondolella prexuanhanensis* – *Jinogondolella*

820 *xuanhanensis*, *J. granti* – *C. postbi* = *Jinogondolella granti* – *Clarkina postbitteri*.

821

822 **Fig. 7.** Stratigraphic variations in the PDS section (a), GD core (b) and QLS section (c) for
823 Cd/Mo, Co×Mn, Mo/TOC, P/Al, and TOC/TP (molar) ratios. The green dashed lines indicate
824 the boundary of Kuhfeng and Yinping Formation, and the red dashed lines represent diagnostic
825 thresholds for proxies of upwelling (after Sweere et al., 2016) and P cycling (after Algeo and
826 Ingall, 2007; Schobben et al., 2020). Data of PDS section and GD core are from Zhang et al.,
827 2021, 2022a.

828

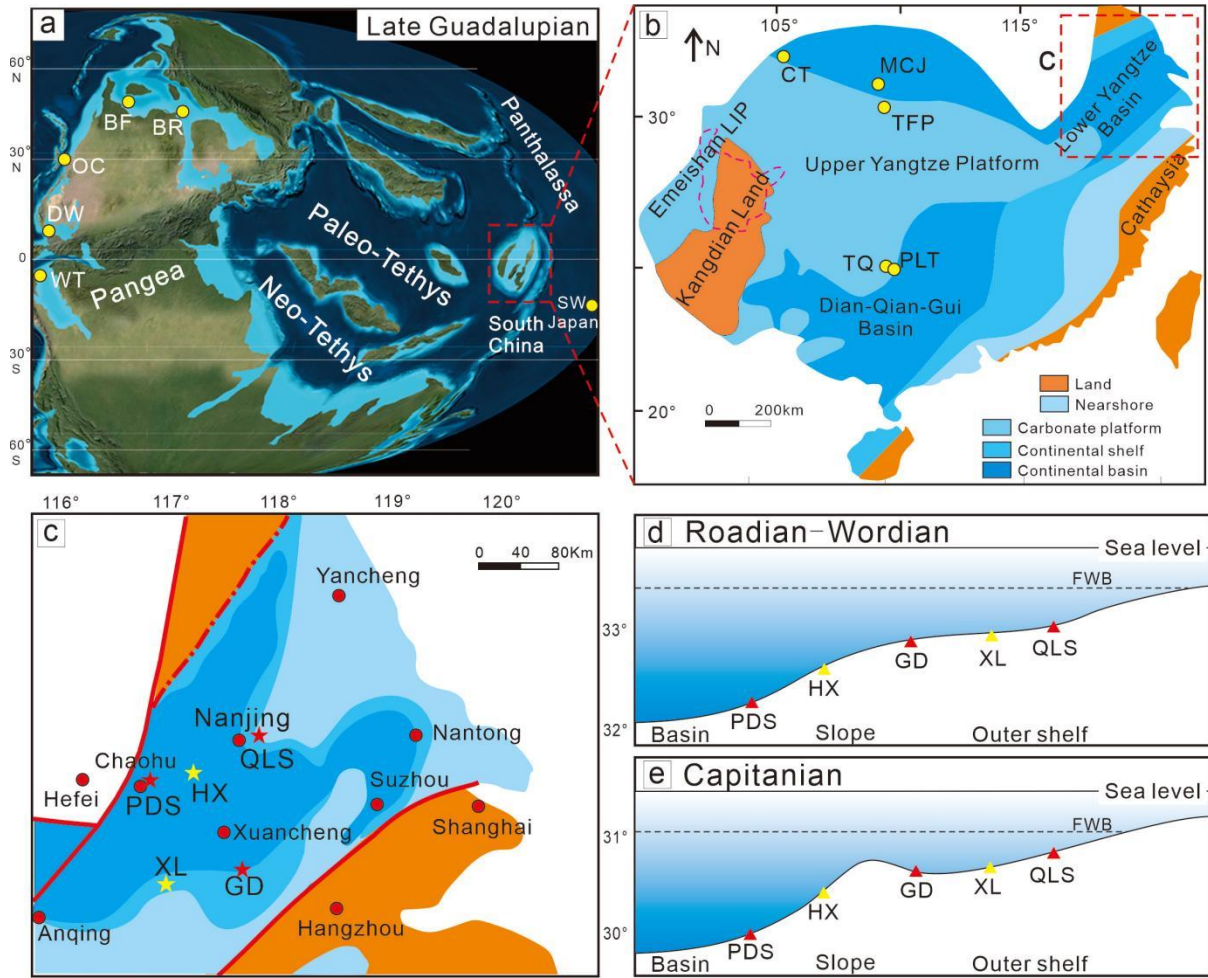
829 **Fig. 8.** Crossplots of Cd vs Mo (a), Co×Mn vs Al (b) for the three studied sections. These basic
830 graphs are modified from Sweere et al. (2016).

831

832 **Fig. 9.** Compilation of global redox records in the context of the Capitanian marine biotic crisis
833 and contemporaneous events. The redox records are from Schoepfer et al., 2013 (OC), Saitoh
834 et al., 2014 (CT), Bond et al., 2015, 2020 (BR and BF), Zhang et al., 2015 (WT and TQ), Shi
835 et al. 2016 (MCJ), Wei et al., 2016, 2019 (PLT, TFP, and XL), Fujisaki et al., 2019 (SW Japan),
836 Zhang et al., 2019a (HX), and Smith et al., 2020 (DW). The paleontological data are
837 summarized from Shen and Shi (2009) and Bond et al. (2010). Events shown are the Emeishan
838 LIP (Wignall et al., 2009), climate warming (Zhang et al., 2021), and regression (Sun et al.,
839 2010; Zhang et al., 2019b).

840

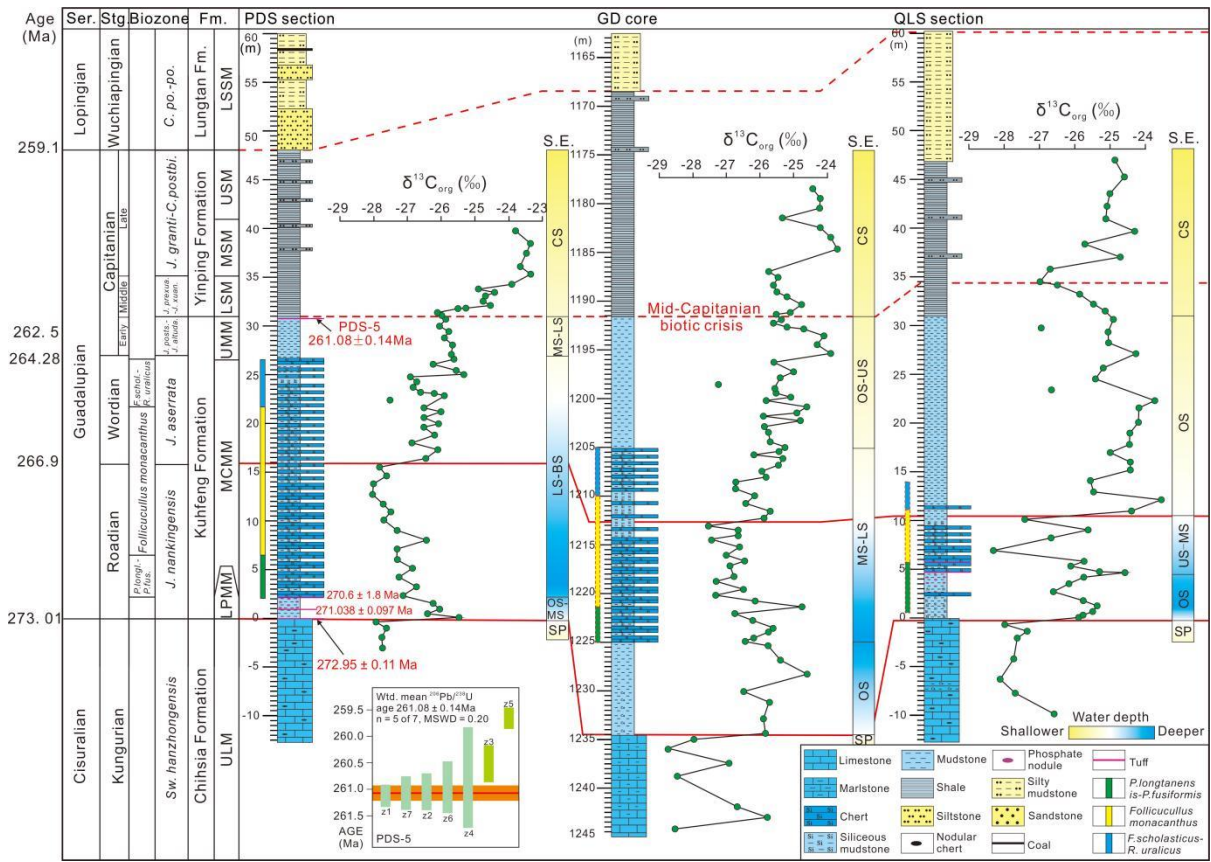
841 **Fig. 1.**



842

843

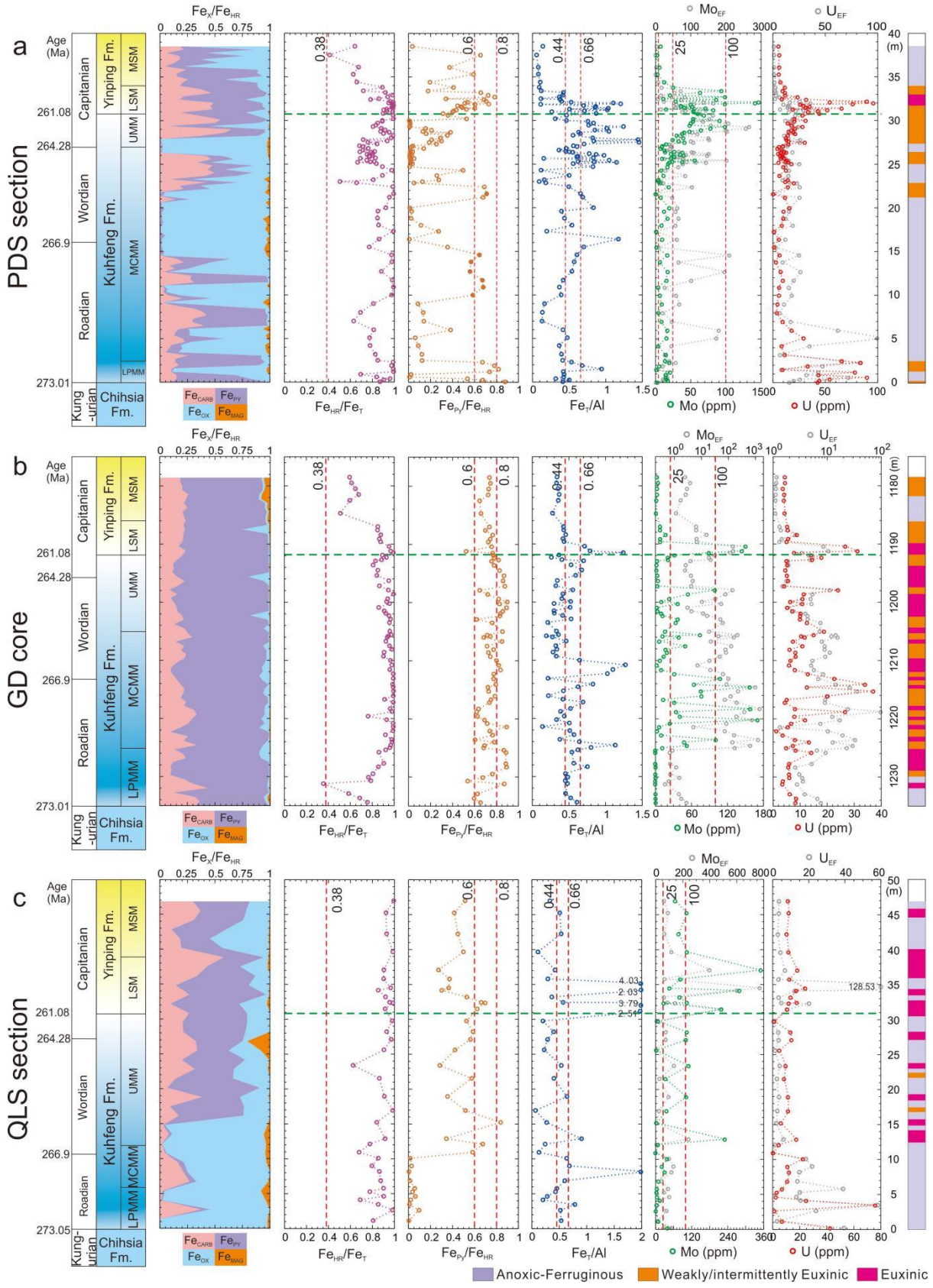
844 Fig. 2.



845

846

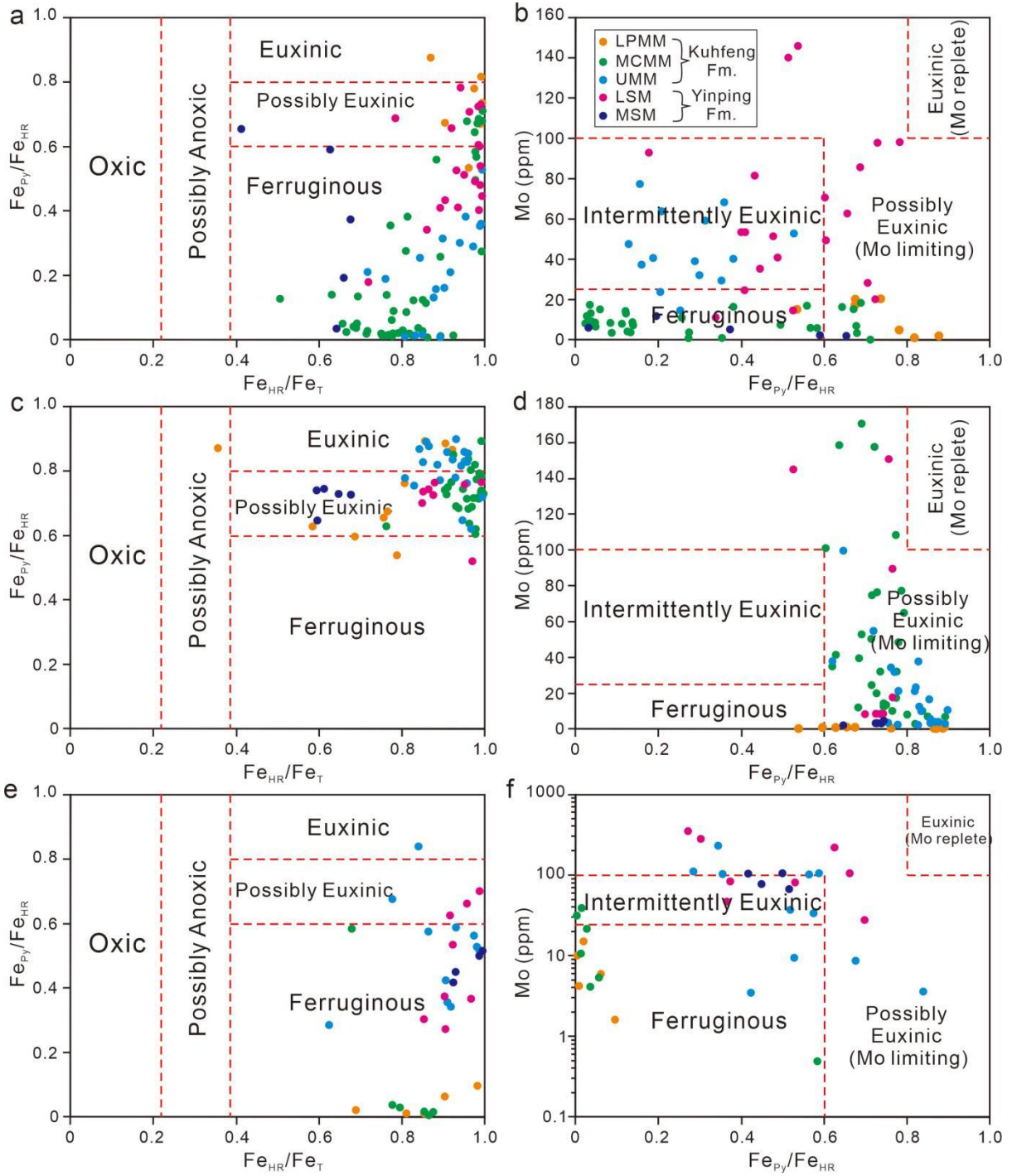
847 **Fig. 3.**



848

849

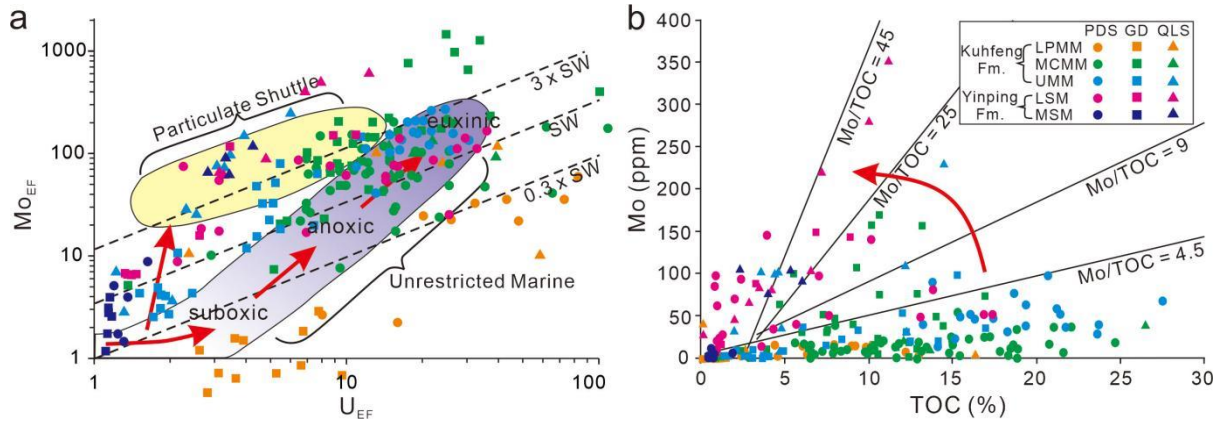
850 **Fig. 4.**



851

852

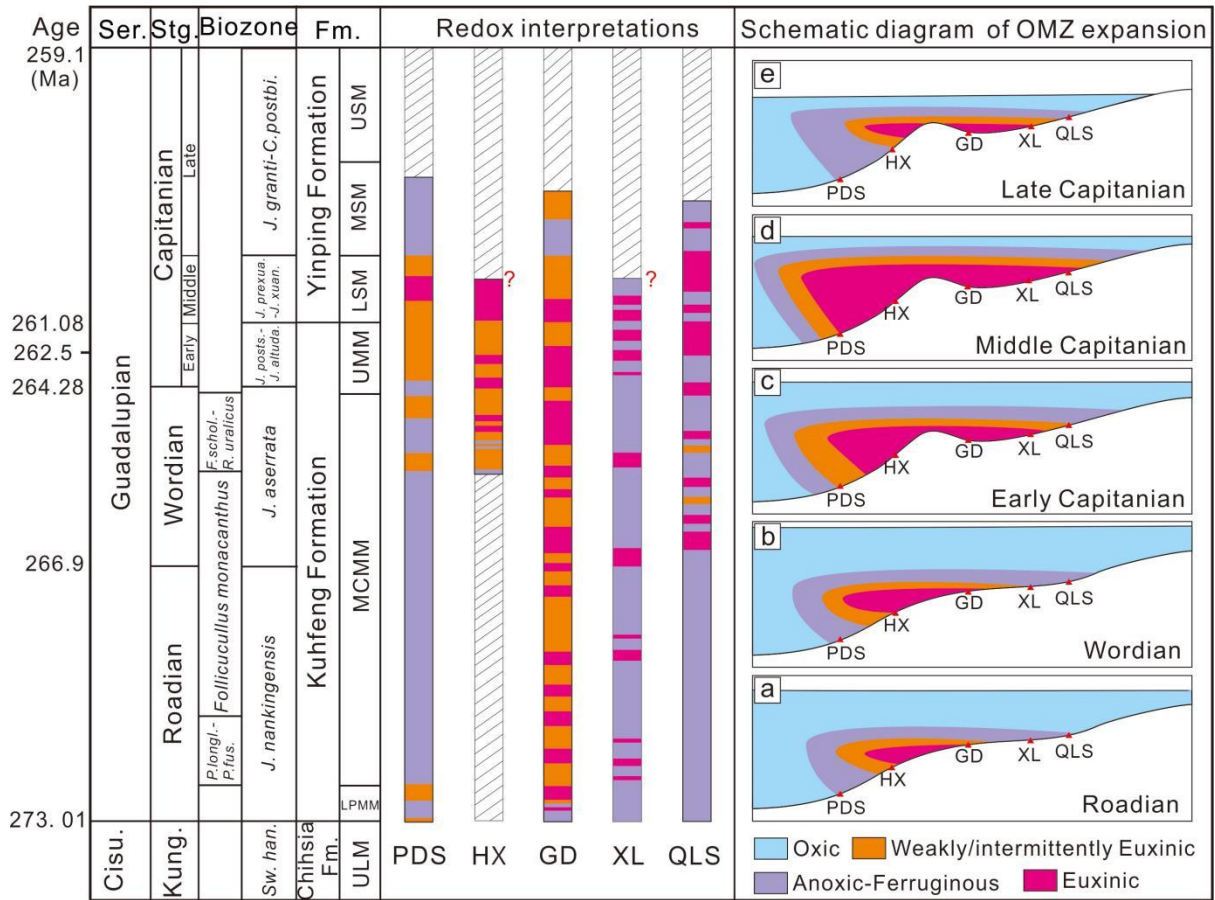
853 **Fig. 5.**



854

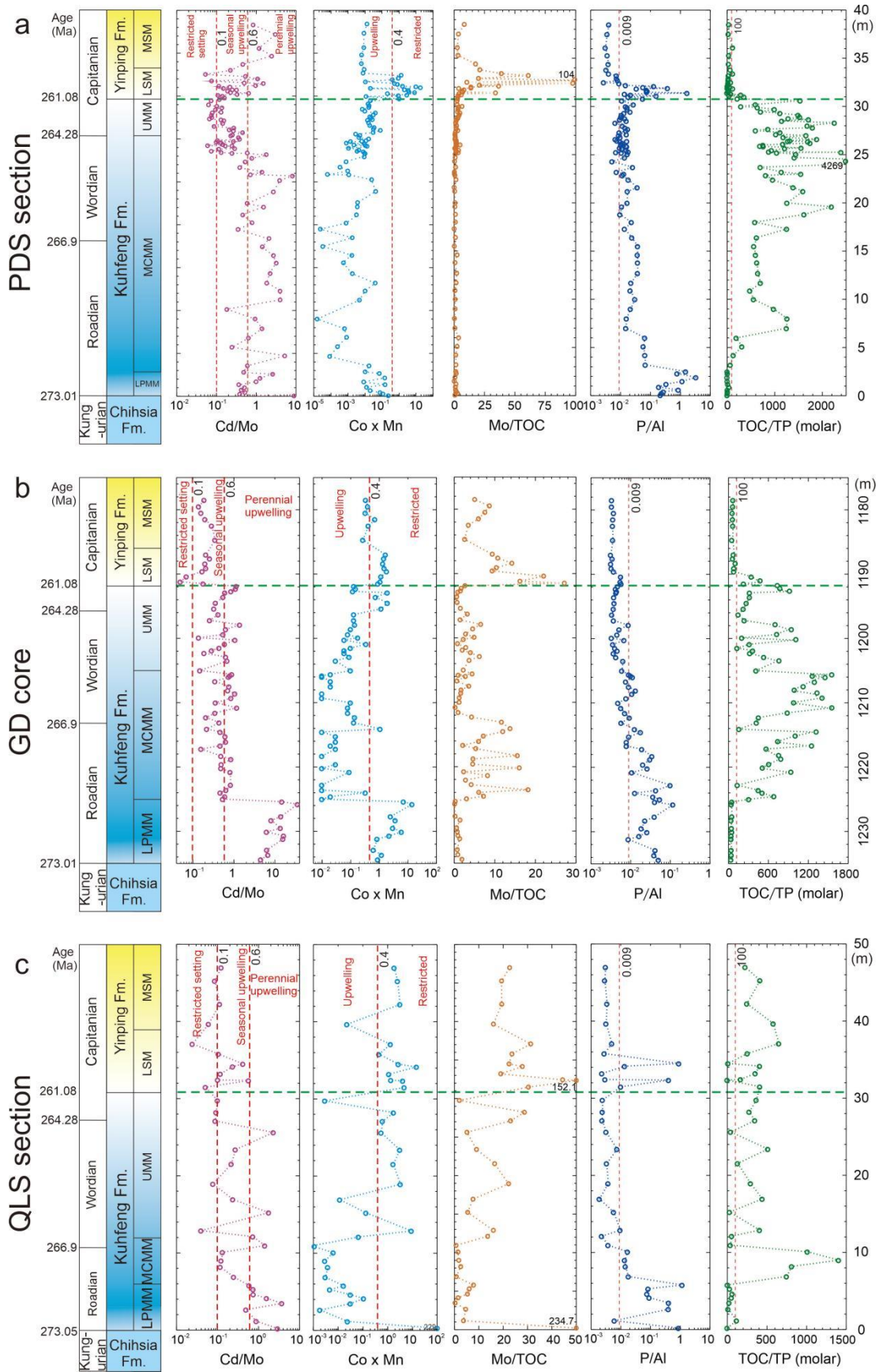
855

856 **Fig. 6.**

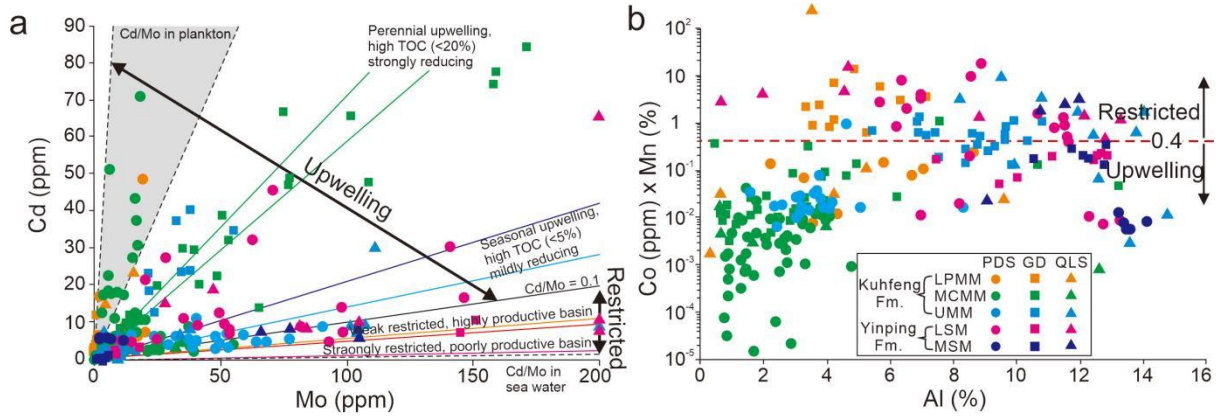


857

858



861 **Fig. 8.**



862

863

Fig. 9.

